AIMS Mathematics

AIMS Mathematics, 11(6): 18801–18834.
DOI: 10.3934/math.2026765
Received: 14 May 2026
Revised: 15 June 2026
Accepted: 18 June 2026
Published: 25 June 2026

https://www.aimspress.com/journal/Math

Research article

Robust fatigue-aware adaptive control via cascaded SMO-UKF estimation for nonlinear systems under uncertainties

Jun-Hee Lee[1], Ganesh Mayilsamy[2], Baek-Soon Kwon[3] and Jae Hoon Jeong[4,*]

[1] Department of Electronic and Information Engineering, Kunsan National University, 558, Daehak-ro, Gunsan, 54150, Jeonbuk, Republic of Korea
[2] School of Electrical Engineering, Vellore Institute of Technolog-Chennai Campus, Kelambakkam-Vandalur Rd, Chennai, 600 127, Tamilnadu, India
[3] School of Mechanical Engineering & Advanced Machinery Technology Research Institute, Kunsan National University, Republic of Korea
[4] Kunsan National University, 558, Daehak-ro, Gunsan, 54150, Jeonbuk, Republic of Korea

* **Correspondence:** Email: jh7129@kunsan.ac.kr; Tel: +82634694702.

Abstract: This paper proposes an adaptive torque control and state estimation method that effectively addresses the trade-off between fatigue load reduction and power generation performance in a nonlinear wind energy conversion system subject to strong turbulence, measurement noise, and model uncertainties. The proposed fatigue load-aware adaptive torque controller dynamically adjusts control weights based on the variability, mismatch, and standard deviation of the aerodynamic torque, thereby reducing drivetrain fatigue loads while minimizing power loss. In addition, to accurately estimate the highly nonlinear and unknown aerodynamic torque, a combined estimator based on SMO and UKF was designed. SMO provides robustness against disturbances and noise, while the UKF enhances estimation accuracy in nonlinear systems, enabling reliable aerodynamic torque estimation. To validate the performance, simulations were conducted under three different turbulence intensities and wind speed profiles. Simulation results demonstrated that the proposed SMO-UKF estimator achieves up to a 2.77% improvement in estimation performance compared to conventional methods. Furthermore, the proposed control strategy reduces fatigue loads by up to 15.52% with negligible reduction in power output.

Keywords: SMO; UKF; torque; adaptive control; wind turbine system
Mathematics Subject Classification: 93C42, 93E10

Nomenclature	
Variables	
P_a, P_e	Aerodynamic power, generator power
T_a, T_e, $\hat{T}_a$, T_e^*	Aerodynamic torque, generator torque, estimated aerodynamic torque, and reference generator torque
ω_m, ω_e, $\hat{\omega}_{smo}$	Rotor speed, generator rotor speed, SMO-based estimated rotor speed
ρ, R_B, β, C_p, λ_{TSR}	Air density, blade radius, blade pitch angle, power coefficient, and tip-speed ratio
v_w	Wind speed
v_d, v_q, i_d, i_q, L_d, L_q	Stator voltages, currents, and inductances in the d–q reference frame
R_p, ψ_{mag}, p_g, J, B	Stator resistance, generator air-gap flux, number of pole pairs, equivalent inertia, viscous friction coefficient
x, P, Q, R	State vector, state covariance matrix, process noise covariance, measurement noise covariance
W, η, K_{UKF}	Process noise, measurement noise, Kalman gain
w_{mppt}, w_{aero}, w_{damp}	Control weighting factors
Abbreviations	
OTC	Optimal torque control
DD-PMSG	Direct-drive permanent magnet synchronous generator
AGTC	Adaptive generator torque control
ADRC	Active disturbance rejection control
BiLSTM	Bidirectional long short-term memory
MPC	Model predictive control
IMU	Inertial measurement unit
DDHO	Deep-dive holistic observer
SMC	Sliding mode control
SMO	Sliding mode observer
UKF	Unscented Kalman filter
MPPT	Maximum power point tracking
DEL	Damage equivalent load
EKF	Extended Kalman filter
DOB	Disturbance observer

1. Introduction

Globally, the share of environmentally friendly energy generation has been steadily increasing, and the proportion of wind energy in modern power systems has grown significantly in recent years [1]. Accordingly, the stable and efficient operation of wind turbines has become increasingly important. In particular, as wind turbines continue to increase in size, structural reliability and maintenance costs have emerged as critical issues [2–4]. Fatigue damage caused by repetitive loads is known to be one of the primary causes of failure [5–7]. In particular, the drivetrain is continuously subjected to loads induced by generator torque fluctuations [8,9], making it one of the most vulnerable components to fatigue damage [10,11]. In general, fatigue loads in wind turbines are evaluated based on the Rainflow counting method and cumulative damage theory, which are widely used to quantitatively analyze the characteristics of cyclic loads [12,13]. Previous studies have proposed fatigue load reduction methods focusing mainly on structural loads such as blade root bending moments and tower base loads. However, these approaches primarily emphasize structural aspects, and research on drivetrain fatigue loads—directly affected by generator torque fluctuations—remains relatively limited [14–16].

The operating conditions of a wind turbine are typically divided into three regions: Region 1 (below the cut-in wind speed, v_{cut-in}), Region 2 (between the cut-in wind speed and the rated wind speed, v_{rated}), and Region 3 (between the rated wind speed and the cut-out wind speed, $v_{cut-out}$). In general, optimal torque control (OTC) is applied in Region 2. However, since this control strategy is designed primarily to maximize power extraction, it does not sufficiently account for drivetrain fatigue loads caused by torque fluctuations [17,18]. In particular, under turbulent wind conditions, torque variability increases, which induces cyclic loads and accelerates fatigue damage in the drivetrain [19]. Therefore, active torque control in Region 2 that can resolve the trade-off between maximizing power production and reducing drivetrain fatigue loads is essential for extending system lifetime and ensuring stable operation.

Meanwhile, wind turbines based on direct-drive permanent magnet synchronous generators (DD-PMSGs) have a structural characteristic of not using a gearbox. As a result, generator torque fluctuations are transmitted directly to the drivetrain without attenuation. Due to this characteristic, the torque controller has a more direct impact on drivetrain fatigue loads, further emphasizing the importance of torque-based fatigue load reduction control strategies [20–23]. The aerodynamic torque T_a acting on a wind turbine is an important physical quantity that directly reflects external disturbances. However, in practical systems, it is difficult to measure T_a directly due to sensor limitations and cost constraints [24–26]. Therefore, most conventional control methods rely on limited measurable variables such as rotor speed ω_m and generator torque T_e, which makes it difficult to accurately capture external disturbances. To overcome these limitations, observer-based state estimation methods have been studied to estimate aerodynamic torque. However, integrated studies that directly utilize the estimated aerodynamic torque in torque controllers for drivetrain fatigue load reduction remain relatively limited [27,28]. Recently, studies on robust adaptive control utilizing event-based control and nonlinear filtering have been reported, and these studies are contributing to the improvement of state estimation and control performance in nonlinear systems [29,30].

In [31], an adaptive generator torque control (AGTC) method was proposed to reduce fatigue loads on the tower and low-speed shaft. However, since the approach was primarily designed for structural load alleviation, it provided limited consideration from the perspective of directly controlling drivetrain torque fluctuations. In [32], a nonlinear torsional vibration damper based on active disturbance rejection control (ADRC) was proposed to effectively suppress drivetrain vibrations in wind turbines. However, this approach focuses on vibration mitigation and is fundamentally different from reducing fatigue loads caused by cyclic loading. In [33], an ADRC-based torque–pitch cooperative control strategy combined with a data-driven fatigue model (BiLSTM) was proposed to simultaneously achieve power tracking performance and fatigue load reduction. However, this study relies on combined control, including pitch control, and depends on data-driven fatigue estimation, limiting its analysis in terms of drivetrain-oriented physical interpretation and single torque control-based load reduction. In [34], the nonlinear wind turbine system was divided into multiple linear models, and a soft-switching-based model predictive control (MPC) was applied to achieve stable control and fatigue load reduction across the entire operating region. However, this method increases controller complexity due to its reliance on multiple models and switching logic and provides limited consideration of model uncertainty and state estimation issues in practical implementations. In [35], wind speed and system states were estimated using a tower-top inertial measurement unit (IMU) and a deep-dive holistic observer (DDHO), and these estimates were applied to MPC to improve power efficiency and reduce fore–aft tower fatigue loads. In [36], a variable-weight MPC strategy was proposed for cooperative control of pitch angle and torque, while [37] introduced a two-degree-of-freedom model-based MPC strategy that simultaneously considers power tracking and fatigue load reduction. However, these control strategies heavily rely on sensor-based state feedback, such as mechanical anemometers or IMUs, which limit their robustness under severe turbulence or sensor fault conditions encountered in real wind turbine operation. To overcome this sensor dependency, [38] proposed a sliding mode observer (SMO)-based approach to estimate drivetrain states and added an auxiliary control input to the generator torque to suppress torsional and blade edgewise vibrations, thereby alleviating fatigue loads. However, this method relies on compensation terms designed for specific structural vibration characteristics, making it difficult to extend into a control framework that comprehensively considers overall drivetrain torque behavior.

To address these limitations, this paper proposes a fatigue load-aware adaptive torque control framework based on a sliding mode observer–unscented Kalman filter (SMO-UKF), which actively reduces torsional fatigue loads in a DD-PMSG drivetrain without the use of wind speed sensors. The objective of this study is to effectively reduce drivetrain fatigue loads induced by generator torque fluctuations while maintaining maximum power point tracking (MPPT) in the operating Region 2. The proposed system consists of an integrated structure that organically links aerodynamic torque estimation and fatigue load reduction control and is largely composed of an SMO-UKF aerodynamic torque estimator and a fatigue load-aware adaptive torque controller.

- SMO-UKF estimator: Since the aerodynamic torque of a wind turbine is difficult to estimate directly and involves strong nonlinearity and uncertainty, a cascaded estimation structure combining SMO and UKF in series was designed to effectively estimate it. First, a rotor speed ω_m, which is robust against measurement noise and disturbances, is estimated using SMO, and this is utilized as an observation for UKF to estimate the aerodynamic torque T_a based on a nonlinear dynamic model. The proposed structure is designed to mitigate the uncertainty of measurement signals and improve the reliability of aerodynamic torque estimation by simultaneously utilizing the robustness of SMO and the nonlinear estimation performance of UKF. Unlike EKF-based estimation techniques, UKF estimates the state using sigma points without Jacobian matrix calculation or linearization processes, thereby effectively reflecting the wind turbine dynamics with strong nonlinearity.
- Fatigue load-aware adaptive torque controller: Unlike conventional torque control techniques that focus on a specific objective—either power generation performance or load reduction—the proposed controller adaptively generates generator torque commands by simultaneously considering the estimated aerodynamic torque change rate, control error, and real-time fatigue load status. It is designed to actively adjust the trade-off between power generation performance and drivetrain fatigue load reduction by reflecting the dynamic characteristics of aerodynamic torque in real time. This allows for the suppression of excessive torque fluctuations while minimizing power output reduction, thereby effectively reducing the fatigue load on the drivetrain.

Existing disturbance observation–based techniques primarily focus on disturbance compensation and do not directly utilize the estimated information for fatigue load reduction control. Additionally, while MPC-based techniques can provide excellent control performance, the computational burden increases due to the iterative online optimization process. On the other hand, the cascaded SMO-UKF structure proposed in this study ensures the reliability of aerodynamic torque estimation while directly reflecting the estimated information in fatigue load-aware adaptive torque control, thereby enabling real-time adjustment of the balance between power generation performance and fatigue load reduction.

To quantitatively evaluate the performance of the proposed control method, the load history of the torque signal was analyzed using the Rainflow counting method, and the damage equivalent load (DEL) was calculated for various Wöhler exponents. The proposed method was validated under three different turbulent wind conditions in a MATLAB/Simulink-based simulation environment, and its performance in reducing drivetrain fatigue loads was evaluated through comparison with conventional torque control methods.

The main contributions of this paper are as follows:

- We propose an integrated framework that organically links aerodynamic torque estimation and adaptive torque control to reduce the fatigue load of wind turbine drivetrains. The proposed structure is designed to consider the trade-off between power generation performance and drivetrain fatigue load by not merely estimating aerodynamic torque information but directly utilizing it in control decision-making.
- We design a cascaded aerodynamic torque estimator that directly combines SMO and UKF. The proposed estimator can effectively reflect nonlinear dynamic characteristics while mitigating the uncertainty of measurement signals, thereby enabling reliable aerodynamic torque estimation even in turbulent environments or under conditions where model uncertainty exists.
- We propose a fatigue-aware adaptive torque control technique that simultaneously reflects aerodynamic torque variability, estimation error, and fatigue load status. Through this, the balance between power generation performance and fatigue load reduction performance can be adjusted in real time according to operating conditions, overcoming the limitations of existing methods that use fixed control targets.
- The proposed system, integrating an estimator and a controller, is applied to a DD-PMSG-based wind power generation system, and the fatigue load reduction effect and practicality are comprehensively verified by performing Rainflow counting and DEL analysis in various turbulent environments.

The remainder of this paper is organized as follows: Section 2 describes the dynamic model of the wind turbine. Section 3 explains the aerodynamic torque estimator. Section 4 presents the proposed torque control strategy, and Section 5 provides fatigue load analysis and simulation results. Finally, Section 6 concludes the paper.

2. Wind turbine system and PMSG modeling

2.1. Wind turbine system and PMSG modeling

In this section, the wind turbine model and the DD-PMSG dynamic model used in this study are presented. Figure 1 illustrates the overall schematic of the proposed control system. The aerodynamic power P_a and aerodynamic torque T_a of the wind turbine can be defined as in (1) and (2), respectively [39–41].

$$P_a = \frac{1}{2}\rho\pi {R_B}^2 C_p(\lambda_{TSR},\beta)V_w = \frac{1}{2{\lambda_{TSR}}^3}\rho\pi {R_B}^5 C_p(\lambda_{TSR},\beta){\omega_m}^3 \tag{1}$$

$$T_a = \frac{1}{2{\lambda_{TSR}}^3}\rho\pi {R_B}^5 C_p(\lambda_{TSR},\beta){\omega_m}^2 \tag{2}$$

$$\lambda_{TSR} = \frac{\omega_m R_B}{V_w} \tag{3}$$

$$C_p(\lambda_{TSR},\beta) = g_1\left(\frac{g_2}{\lambda_i} - g_3\beta - g_4\right) exp^{-g_5/\lambda_i} + g_6\lambda_{TSR} \tag{4}$$

$$\lambda_i = \frac{1}{\lambda_{TSR}+g_7\beta} - \frac{g_8}{\beta^3+1}. \tag{5}$$

Here, ρ denotes the air density, R_B is the blade radius, V_w represents the wind speed, and ω_m is the rotor speed. The power coefficient C_p represents the efficiency with which a wind turbine converts incoming wind energy into mechanical energy, being a nonlinear function determined by λ_{TSR} and β. The power coefficient $C_p(\lambda_{TSR},\beta)$ is determined by the tip speed ratio λ_{TSR} and the blade pitch angle β. The tip speed ratio λ_{TSR} is defined as the ratio between the rotational speed of the blade tip and the wind speed, as given in (3). The C_p model used in this study is expressed as in (4) and (5) [39–41]. In this case, $g_1 = 0.5176$, $g_2 = 116$, $g_3 = 0.4$, $g_4 = 5$, $g_5 = 21$, $g_6 = 0.0068$, $g_7 = 0.08$, and $g_8 = 0.035$.

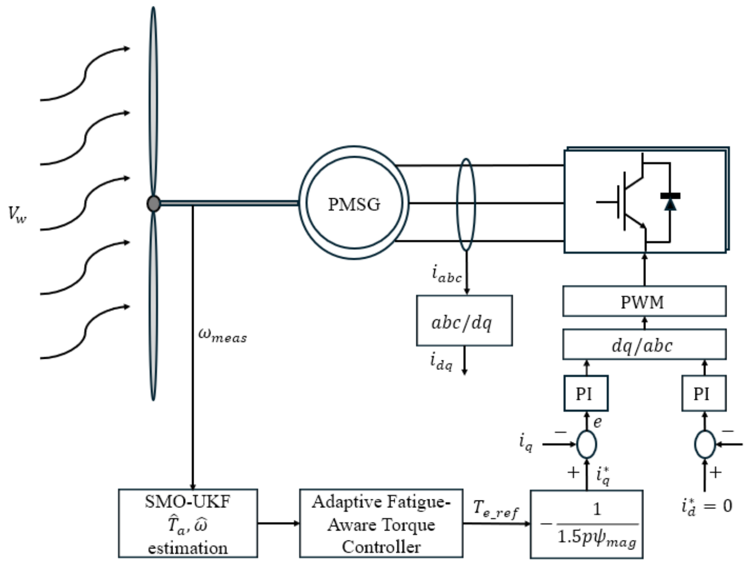

Figure 1. Schematic diagram of the overall DD-PMSG-based wind turbine system.

The generator is modeled as a PMSG in the dq-axis reference frame. To describe the operation of the PMSG, both electrical and mechanical dynamics are considered. The stator voltages v_d and v_q are modeled as (6) and (7) [39–41].

$$v_d = R_p i_d + L_d \frac{di_d}{dt} - \omega_e L_q i_q \tag{6}$$

$$v_q = R_p i_q + L_q \frac{di_q}{dt} - \omega_e L_d i_d + \omega_e \psi_{mag} \tag{7}$$

$$T_e = -1.5 p_g \psi_{mag} i_q \tag{8}$$

$$P_e = -1.5\left(v_q i_q + v_d i_d\right). \tag{9}$$

Here, R_p is the stator resistance, i_d and i_q are the dq-axis generator currents, L_d and L_q are the inductances, and ψ_{mag} is the generator air-gap flux. The electrical angular speed is given by $\omega_e = p_g\omega_m$, where p_g denotes the number of pole pairs. The generator torque T_e is determined by the q-axis current i_q and is defined as in (8), while the generator output power P_e is defined as in (9) [39–41].

$$\frac{d}{dt}\omega_m = \frac{1}{J}(T_a - T_e - B\omega_m). \tag{10}$$

To represent the mechanical dynamics between the wind turbine and the generator, the drivetrain is modeled as a one-mass system, as defined in (10). Here, J denotes the equivalent inertia, and B represents the viscous damping coefficient.

2.2. Operating range and output characteristics of wind turbine systems

The wind turbine system exhibits different operating characteristics depending on wind speed conditions and is generally divided into three operating regions. Figure 2 shows the operating regions of the wind turbine system used in this paper, where the cut-in wind speed v_{cut-in} is defined as 3 m/s, the rated wind speed v_{rated} is 11 m/s, and the cut-out wind speed $v_{cut-out}$ is 22.5 m/s. The first region (Region 1) corresponds to wind speeds below v_{cut-in}, where the turbine cannot generate sufficient aerodynamic torque, and thus no power is produced. The second region (Region 2) lies between the cut-in wind speed v_{cut-in} and the rated wind speed v_{rated}, and its objective is to extract maximum power from the wind. In this region, generator torque control dominates the system operation instead of blade pitch control. By regulating the rotor speed ω_m, the tip speed ratio λ_{TSR} is maintained at its optimal value, thereby achieving the maximum power coefficient. In general, the optimal torque control (OTC) method is applied, being defined as in (11) [20].

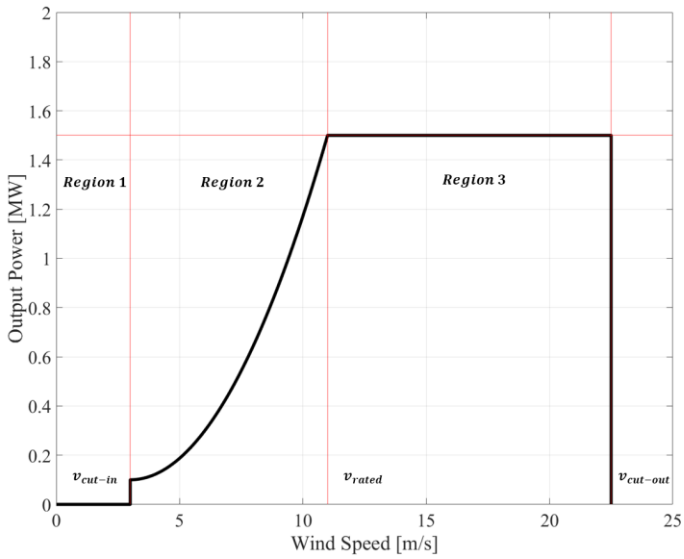

Figure 2. Wind turbine system operating range.

$$T_e^* = K_{opt} * {\omega_m}^2 \tag{11}$$

$$K_{opt} = \frac{1}{2}\rho\pi {R_B}^5 \frac{C_p^{max}}{{\lambda_{opt}}^3}. \tag{12}$$

Here, K_{opt} is a constant determined by turbine parameters and is defined as in (12). In this study, $C_p^{max} = 0.48$ and $\lambda_{opt} = 8.1$. In particular, the OTC-based MPPT method is widely used due to its simple structure and high practicality. However, irregular variations in wind speed cause fluctuations in generator torque, which impose cyclic loads on the drivetrain and increase fatigue damage. The third region (Region 3) corresponds to wind speeds between v_{rated} and $v_{cut-out}$, where the output power of the wind turbine is limited through blade pitch control to prevent it from exceeding the rated value [20]. Therefore, considering these operating characteristics, this paper proposes a control strategy that reduces drivetrain fatigue loads by mitigating torque fluctuations while maintaining MPPT performance in Region 2.

3. SMO-UKF estimator

In this study, an SMO-UKF observer was designed to estimate aerodynamic torque, and Figure 3 shows a schematic diagram of the SMO-UKF. First, SMO is robust against model uncertainty and disturbances, and provides fast convergence characteristics, especially in environments with unknown inputs such as aerodynamic torque [26]. However, since SMO includes switching terms, chatter may occur, and it may have limitations in terms of accuracy when used alone. On the other hand, UKF provides high estimation accuracy by probabilistically propagating the state distribution of a nonlinear system and has the advantage of effectively reflecting system dynamics. However, estimation performance may be degraded due to a relative lack of robustness against measurement noise, modeling errors, and disturbances [28]. Considering the characteristics of each technique, this study designed a cascaded SMO-UKF observer by serially combining SMO and UKF with the super-twisting technique and applying a saturation function. At this time, the UKF was constructed with reference to [42], and the SMO was utilized as a preprocessing estimator for the UKF rather than a simple state observer. Specifically, the measured rotor speed ω_{meas} is input into the SMO to generate a speed estimate with the influence of disturbances and measurement noise mitigated, which is used as an observation for the UKF. This prevents the UKF from being directly exposed to raw measurement signals, thereby enabling stable and reliable state estimation. Furthermore, unlike EKF-based estimation techniques that rely on Jacobian matrix calculations and local linearization processes, the UKF uses an unscented transformation to directly propagate nonlinear states, allowing it to effectively reflect linear dynamics without Jacobian calculations [42]. Therefore, the nonlinear characteristics of the system can be effectively estimated even in wind turbine systems where operating conditions change continuously due to turbulent environments. Consequently, by having SMO perform robust preprocessing estimation and UKF perform stochastic correction reflecting nonlinear dynamics based on this, the accuracy and reliability of aerodynamic torque estimation can be simultaneously improved even in environments where measurement noise, disturbances, and model uncertainty exist. Here, T_e represents the generator torque calculated from the measured current and includes measurement noise and parameter uncertainty.

As a result, the proposed SMO-UKF has the following advantages:

- Robustness against disturbances and model uncertainties.
- Reduced impact of measurement noise through SMO-based pre-estimation.
- High estimation accuracy in nonlinear systems.
- Stable estimation performance and fast convergence through the cascaded structure.

By combining the SMO and UKF, the SMO-UKF compensates for the limitations of each method, thereby providing high estimation performance in environments with strong nonlinearity and uncertainty, such as wind turbine systems.

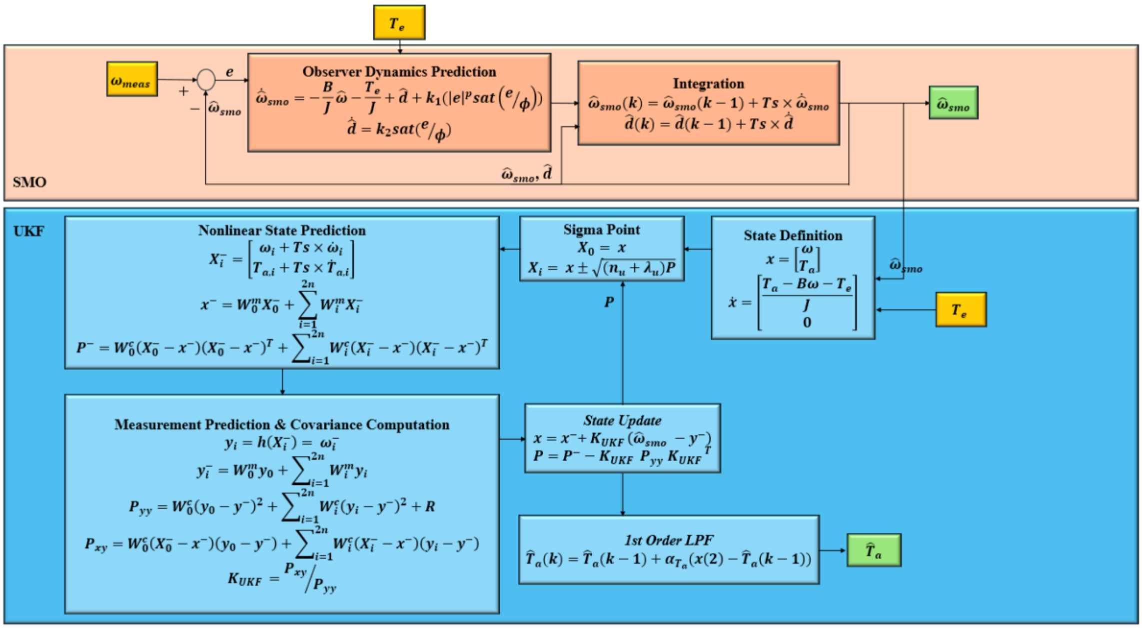

Figure 3. SMO-UKF schematic diagram.

3.1. SMO-UKF estimator design

The rotor dynamics of the wind turbine are defined as in (10), and the nonlinear sliding function is defined as in (14). Here, $0 < p < 1$, and the estimation error e and the saturation function $sat(e)$ are defined as in (15) and (16), respectively.

$$s(e) = |e|^p sat(e) \tag{14}$$

$$e = \omega_{meas} - \widehat{\omega}_{smo} \tag{15}$$

$$sat(e) = \begin{cases} 1, & e > \phi \\ e/\phi, & |e| \leq \phi. \\ -1, & e < -\phi \end{cases} \tag{16}$$

Here, ω_m denotes the rotor speed, $\widehat{\omega}_{smo}$ is the rotor speed estimated by the SMO, and ϕ represents the boundary layer. The $|e|^p$ term in the nonlinear sliding function ensures sufficient convergence speed even when the error is small, thereby achieving finite-time convergence characteristics. The saturation function $sat(e)$ is adopted to alleviate the chattering phenomenon. The dynamics of the SMO-based speed estimation and the disturbance estimation law are given in (17) and (18), respectively.

$$\dot{\widehat{\omega}}_{smo} = -\frac{B}{J}\widehat{\omega}_{smo} - \frac{T_e}{J} + \hat{d} + k_1 s(e) \tag{17}$$

$$\dot{\hat{d}} = k_2 sat(e). \tag{18}$$

Here, $\hat{d}$ denotes the estimated disturbance corresponding to the aerodynamic torque, and k_1 and k_2 represent the observer gains. Based on the SMO-estimated rotor speed $\widehat{\omega}_{smo}$, the UKF performs precise estimation of the aerodynamic torque. The state vector and the state equation are defined as in (19) and (20), respectively.

$$x = \begin{bmatrix} \omega_m \\ T_a \end{bmatrix} \tag{19}$$

$$\dot{x} = \begin{bmatrix} \frac{T_a - B\omega_m - T_e}{J} \\ 0 \end{bmatrix} + W. \tag{20}$$

Here, W represents the process noise, which probabilistically accounts for uncertainties such as turbulence-induced fluctuations, unmodeled dynamics, and variations in system parameters. The rotor speed $\widehat{\omega}_{smo}$ estimated by the SMO is used as the measurement in the UKF, and the measurement equation is defined as in (21).

$$y = \widehat{\omega}_{smo} = \omega_m + \eta. \tag{21}$$

Here, ω_m denotes the rotor speed, and η represents the equivalent measurement noise that includes estimation error.

When UKF is applied to a nonlinear system, the state is estimated as follows:
Sigma point generation:

$$X_i = x \pm \sqrt{(n_u + \lambda_u)P}. \tag{22}$$

Here, X_i denotes the i-th sigma point, n_u is the dimension of the state vector, λ_u is the UKF scaling parameter, and P represents the state covariance. For $i = 1, \cdots, n$ the upper and lower sigma points are constructed, and the sigma points are generated using the current state estimate and covariance.

Nonlinear state prediction:

In the state prediction step, the system dynamics are applied to each sigma point to propagate the state. Considering the rotor dynamics of the wind turbine, each sigma point can be computed as follows:

$$\omega_i^- = \omega_i + Ts \times \frac{T_{a,i} - B\omega_i - T_e}{J} \tag{23}$$

$$T_{a,i}^- = T_{a,i}. \tag{24}$$

Here, Ts denotes the sampling time. Accordingly, the predicted sigma points are defined as in (25).

$$X_i^- = \begin{bmatrix} \omega_i + Ts \times \frac{T_{a,i} - B\omega_i - T_e}{J} \\ T_{a,i} \end{bmatrix}. \tag{25}$$

Subsequently, the predicted state and covariance are calculated as follows using the weighted mean:

$$x^- = W_0^m X_0^- + \sum_{i=1}^{2n} W_i^m X_i^- \tag{26}$$

$$P^- = W_0^c (X_0^- - x^-)(X_0^- - x^-)^T + \sum_{i=1}^{2n} W_i^c (X_i^- - x^-)(X_i^- - x^-)^T + Q. \tag{27}$$

Here, W_i^m and W_i^c denote the weights of the sigma points. $Q = diag(Q_\omega, Q_{T_a})$ represents the process noise covariance, where Q_ω and Q_{T_a} denote the process noise variances of the rotor speed and aerodynamic torque, respectively.

Measurement prediction and covariance calculation:

$$y_i = h(X_i^-) = \omega_i^- \tag{28}$$

$$y_i^- = W_0^m y_0 + \sum_{i=1}^{2n} W_i^m y_i \tag{29}$$

$$P_{yy} = W_0^c (y_0 - y^-)^T + \sum_{i=1}^{2n} W_i^c (y_i - y^-)^T + R \tag{30}$$

$$P_{xy} = W_0^c (X_0^- - x^-)(y_0 - y^-) + \sum_{i=1}^{2n} W_i^c (X_i^- - x^-)(y_i - y^-) \tag{31}$$

$$K_{UKF} = {}^{P_{xy}}\!/_{P_{yy}}. \tag{32}$$

Here, $h(\cdot)$ is the measurement function that maps the state vector to the measurement space and is defined as a function that outputs the rotor speed. R denotes the measurement noise covariance, representing the measurement uncertainty including the SMO estimation error.

State update and output:

$$x = x^{-} + K_{UKF}\,(\widehat{\omega}_{smo} - y^{-}) \tag{33}$$

$$P = P^{-} - K_{UKF}\;P_{yy}\;{K_{UKF}}^{T} \tag{34}$$

$$\hat{T}_a(k) = \hat{T}_a(k-1) + \alpha_{T_a}(x(2) - \hat{T}_a(k-1)). \tag{35}$$

Here, the rotor speed estimate $\widehat{\omega}_{smo}$ obtained from the SMO is used as the measurement input for the UKF, and y^{-} denotes the mean of the predicted measurements generated from the sigma points. Finally, using the SMO-estimated rotor speed $\widehat{\omega}_{smo}$ as the measurement, the UKF updates the state vector x and covariance P. The aerodynamic torque component of the state vector is then refined through a first-order low-pass filter and provided as the final output T_a. This enables robust and stable aerodynamic torque estimation against noise. Here, α_{T_a} is the low pass filter (LPF) coefficient.

3.2. SMO-UKF estimator stability verification

In this paper, the rotor speed ω_m is estimated using an SMO. The wind turbine dynamics, the error between the actual and estimated speeds, the sliding function, the saturation function, the speed estimation dynamics, and the disturbance estimation law are defined in (10) and (14)–(18).

$$\dot{e} = \dot{\omega}_m - \dot{\widehat{\omega}}_{smo} \tag{36}$$

$$\dot{e} = \frac{T_a}{J} - \hat{d} - k_1 s(e) - \frac{B}{J}e \tag{37}$$

$$\dot{e} = d - \hat{d} - k_1 s(e) - \frac{B}{J}e. \tag{38}$$

The derivative of the error can be defined as in (36), and by substituting (10) and (17) into (36), (37) can be obtained. Defining the disturbance as $d = \frac{T_a}{J}$, (38) is obtained.

$$\tilde{d} = d - \hat{d} \tag{39}$$

$$\dot{e} = \tilde{d} - k_1 s(e) - \frac{B}{J}e \tag{40}$$

$$\dot{\tilde{d}} = \dot{d} - k_2 sat(e). \tag{41}$$

If the disturbance estimation error is defined as in (39), then (40) and (41) can be obtained.

$$\left|\dot{d}(t)\right| \leq L. \tag{42}$$

The aerodynamic torque is a nonlinear function that includes wind speed, rotor speed, and pitch angle, and its rate of change is limited due to the physical constraints of these variables. Therefore, as shown in (42), the disturbance has a bounded rate of change with respect to time. Here, L is a positive constant, and since wind turbines have large inertia, the rate of change of $d = {}^{T_a}\!/_{J}$ is very small.

Theorem:

Assuming that (42) is satisfied, if the observer gains satisfy $k_1 > 0$ and $k_2 > L$, then the estimation error $e(t)$ and the disturbance estimation error $\tilde{d}(t)$ are uniformly ultimately bounded for all time and converge to a finite region around the origin.

Proof:

The stability is proven by dividing the system into two regions based on the saturation function.

Phase 1: Large error region - $|e| > \phi$

In this region, (43) is satisfied.

$$sat(e) = sign(e). \tag{43}$$

Therefore, the error dynamics and the disturbance estimation law can be summarized as (44) and (45), and if (42) is satisfied, then (46) holds.

$$\dot{e} = \tilde{d} - k_1|e|^p sign(e) - \frac{B}{J}e \tag{44}$$

$$\dot{\tilde{d}} = \dot{d} - k_2 sign(e) \tag{45}$$

$$\left|\dot{\tilde{d}}\right| \leq L + k_2. \tag{46}$$

Therefore, since $\dot{\tilde{d}}$ is bounded, $\left|\dot{\tilde{d}}\right|$ is also bounded, which implies that there exists a finite constant D such that $\left|\tilde{d}(t)\right| \leq D$.

The Lyapunov candidate function is defined as in (47), and its derivative is given by (48) [43].

$$V_1 = \frac{1}{2}e^2 \tag{47}$$

$$\dot{V}_1 = e\dot{e} = e\tilde{d} - k_1|e|^{p+1} - \frac{B}{J}e^2. \tag{48}$$

Using boundedness, $\left|e\tilde{d}\right| \leq |e|D$ can be defined. Therefore, (49) is satisfied.

$$\dot{V}_1 \leq |e|D - k_1|e|^{p+1} - \frac{B}{J}e^2. \tag{49}$$

For sufficiently large e, condition (51) is satisfied according to (50), so the error decreases and enters the region $|e| \leq \phi$ within a finite time.

$$|e| > \left(\frac{D}{k_1}\right)^{1/p} \rightarrow D - k_1|e|^p < 0 \tag{50}$$

$$\dot{V}_1 < 0. \tag{51}$$

Phase 1 persists only over a finite time interval. Since $\left|\dot{\tilde{d}}\right| \leq L + k_2$, the disturbance estimation error remains bounded during this interval. Therefore, there exists a positive constant $D > 0$ such that $\left|\tilde{d}(t)\right| \leq D$. In the region where the error is large, the growth rate of the nonlinear damping term dominates the disturbance term, and if condition $0 < p < 1$ is satisfied, the reaching time for the system to enter the boundary layer is finite [44]. For the system to enter the region $|e| \leq \phi$ within a finite time, condition (52) must be satisfied.

$$\left(\frac{D}{k_1}\right)^{1/p} \leq \phi \rightarrow k_1 \geq \frac{D}{\phi^p}. \tag{52}$$

Therefore, the control gain k_1 must be designed sufficiently large to satisfy the above condition, ensuring the transition from Phase 1 to Phase 2.

Phase 2: Boundary layer - $|e| \leq \phi$

In this region, the saturation function is defined as in (53).

$$sat(e) = \frac{e}{\phi}. \tag{53}$$

Therefore, the error dynamics and the disturbance estimation law can be defined as in (54) and (55).

$$\dot{e} = \tilde{d} - k_1 \frac{|e|^p e}{\phi} - \frac{B}{J} e \tag{54}$$

$$\dot{\tilde{d}} = \dot{d} - k_2 \frac{e}{\phi}. \tag{55}$$

In state-space form, the state vector can be expressed as follows:

$$X = \begin{bmatrix} e \\ \tilde{d} \end{bmatrix}, \quad \dot{X} = A(e)X + D(t) \tag{56}$$

$$A(e) = \begin{bmatrix} -\left(\frac{B}{J} + \frac{k_1 |e|^p}{\phi}\right) & 1 \\ -\frac{k_2}{\phi} & 0 \end{bmatrix}, \; D(t) = \begin{bmatrix} 0 \\ \dot{d}(t) \end{bmatrix}. \tag{57}$$

Using the uniform Hurwitz property, (58) and (59) can be obtained within the boundary layer, and the characteristic equation is defined as in (60) [24].

$$|e| \leq \phi \rightarrow |e|^p \leq \phi^p \tag{58}$$

$$\frac{B}{J} \leq \frac{B}{J} + \frac{k_1 |e|^p}{\phi} \leq \frac{B}{J} + k_1 \phi^{p-1} \tag{59}$$

$$\psi^2 + a(e)\psi + b = 0, \; a(e) \geq \frac{B}{J} > 0, \; b = \frac{k_2}{\phi} > 0. \tag{60}$$

Here, the matrix $A(e)$ is continuous and bounded for $|e| \leq \phi$, and since both $a(e)$ and b are positive, it satisfies the second-order Hurwitz condition. Furthermore, since $a(e)$ has a positive lower bound, $A(e)$ is uniformly Hurwitz for all $|e| \leq \phi$ [43]. The disturbance input satisfies (61). Therefore, according to the standard result for systems with a uniformly Hurwitz matrix and bounded input, (62) is satisfied, and the states converge to a finite region around the origin, i.e., the system is uniformly ultimately bounded.

$$|\dot{d}| \leq L \rightarrow \|D(t)\| \leq L \tag{61}$$

$$\|X(t)\| \leq M e^{-\alpha t} \|X(0)\| + \frac{ML}{\alpha}. \tag{62}$$

In conclusion, in Phase 1, the error enters the boundary layer $|e| \leq \phi$ within a finite time, and in Phase 2, the system converges to a uniformly ultimately bounded (UUB) state. Therefore, both $e(t)$ and $\tilde{d}(t)$ are bounded for all time in the overall system and satisfy the UUB property. In addition, since SMO provides a bounded estimate $\hat{\omega}_{smo}$ for rotational speed, the signal ultimately maintains boundedness because the boundedness of the SMO estimation error is established under finite disturbances. Consequently, the output of SMO is used as a finite input for UKF. Assuming that process and measurement noises are finite and the covariance matrices Q_ω, Q_{T_a}, and $\boldsymbol{R}$ are appropriately selected, the UKF estimation error ultimately maintains boundedness [42]. Thus, since SMO guarantees a finite intermediate signal and UKF maintains boundedness under finite inputs, all estimation signals of the cascaded SMO-UKF estimator are uniformly ultimately bounded, so the estimation error does not diverge over time and is confined within a finite vicinity of the origin.

4. Fatigue load-aware adaptive torque controller

4.1. Fatigue load-aware adaptive torque controller design

This section describes a fatigue load-aware adaptive torque controller designed to simultaneously consider wind turbine power efficiency and drivetrain load reduction, and Figure 4 illustrates the schematic of the proposed controller. The proposed controller is formulated as a weighted sum structure that simultaneously accounts for maximum power tracking, aerodynamic torque tracking, and torque fluctuation suppression, and is defined as in (63).

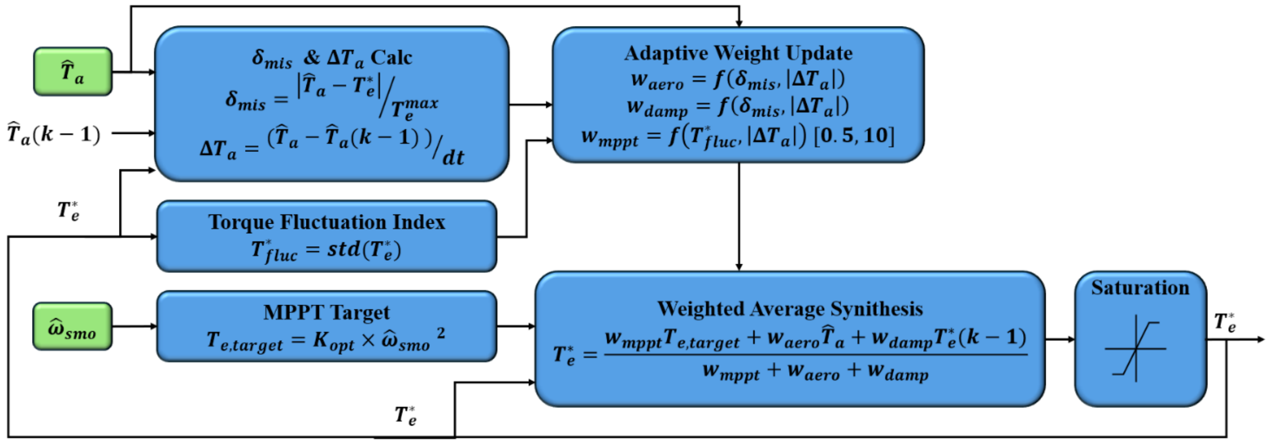

Figure 4. Schematic diagram of a fatigue load-aware adaptive torque controller.

$$T_e^* = \frac{w_{mppt} T_{e,target} + w_{aero} \hat{T}_a + w_{damp} T_e^*(k-1)}{w_{mppt} + w_{aero} + w_{damp}}. \tag{63}$$

Here, $T_{e,target} = K_{opt}\omega^2$, where K_{opt} is a constant determined by the turbine characteristics. $\hat{T}_a$ is the estimated aerodynamic torque, $T_e^*(k-1)$ is the generator torque at the previous time step, and w_{mppt}, w_{aero}, and w_{damp} are the weighting factors for each objective. The key idea of the proposed controller is to adaptively adjust the weights in real time according to the system state. Equation (64) represents the mismatch between the current aerodynamic torque and generator torque, while (65) represents the dynamic variation of the disturbance.

$$\delta_{mis} = |\hat{T}_a - T_e^*| \Big/ T_e^{max} \tag{64}$$

$$\Delta T_a = (\hat{T}_a - \hat{T}_a(k-1)) \Big/ dt. \tag{65}$$

Here, dt denotes the sampling time.

Each weighting factor is defined as follows:

$$w_{aero} = 0.05 + \alpha_{1,aero}\delta_{mis} + \alpha_{2,aero}\frac{|\Delta T_a|}{T_e^{max}} \tag{66}$$

$$w_{damp} = 80 - \alpha_{1,damp}\delta_{mis} - \alpha_{2,damp}\frac{|\Delta T_a|}{T_e^{max}}. \tag{67}$$

Here, $\alpha_{1,aero}$, $\alpha_{2,aero}$, $\alpha_{1,damp}$, and $\alpha_{2,damp}$ are design parameters, and T_e^{max} is the maximum allowable generator torque. Weights are proposed as $w_{areo} \in [0.05, 1]$ and $w_{areo} \in [40, 80]$ to ensure stable operation. When the δ_{mis} increases, w_{aero} increases while w_{damp} decreases, thereby enhancing aerodynamic torque tracking performance. In addition, when the rate of change of aerodynamic torque increases, the sensitivity to disturbances increases, leading to a faster dynamic response.

The fatigue load is approximately evaluated using the standard deviation, $std(.)$, of recent torque history, and a moving standard deviation is calculated over a sliding window of N_{hist} samples.

$$T_{fluc}^{*} = std(T_e^{*}). \tag{68}$$

Based on this, w_{mppt} is adjusted as follows:

$$w_{mppt} = w_0 - \alpha_{1,mppt}\frac{T_{fluc}^{*}}{S} + \alpha_{2,mppt}\frac{|\Delta T_a|}{T_e^{max}}. \tag{69}$$

Here, S is a normalization constant, $\alpha_{1,mppt}$, $\alpha_{2,mppt}$ are design parameters, and T_e^{max} is the maximum value of the generator torque. $w_{mppt} \in [0.5, 10]$ is constrained to ensure stable operation. In this study, adaptive weights were designed using the discrepancy between aerodynamic torque and generator torque δ_{mis}, the rate of change of aerodynamic torque ΔT_a and the standard deviation of torque fluctuation T_{fluc}^{*} as indicators representing the current operating condition. Since increasing values of δ_{mis} and ΔT_a indicate that the wind turbine deviates from steady-state operation, w_{aero} was designed to increase in order to more strongly reflect the estimated aerodynamic torque information. Conversely, w_{damp} was designed to decrease under the same conditions to increase the contribution of aerodynamic torque-based control and enable flexible responses to varying wind speed conditions. Additionally, w_{mppt} was designed to decrease when the torque fluctuation indicator T_{fluc}^{*} increases, since prioritizing MPPT tracking performance under excessive torque fluctuations may lead to increased fatigue loads. On the other hand, when the rate of change of aerodynamic torque $|\Delta T_a|$ increases, the MPPT weight is partially maintained to prevent a rapid degradation in power generation performance. Consequently, the proposed adaptive weighting structure achieves a balance between power generation performance and fatigue load reduction by dynamically adjusting the relative weights of MPPT performance, aerodynamic torque tracking performance, and torque fluctuation suppression according to operating conditions.

The proposed controller has the following advantages over conventional single-objective controllers.

- Simultaneously, three conflicting objectives (maximum power tracking, aerodynamic torque tracking, and fatigue load reduction) within a unified framework.
- Automatically adjusts the weighting factors for each objective based on real-time indicators.
- Directly incorporates the rate of change of aerodynamic torque, thereby accounting for both the magnitude and dynamics of disturbances, enabling fast torque tracking under rapid wind variations and turbulent conditions.
- Effectively reduces structural fatigue loads by incorporating a DEL estimate based on the standard deviation of torque history into the controller and including the previous torque in the control input.

Therefore, the proposed controller can simultaneously achieve power generation efficiency, disturbance rejection performance, and fatigue load reduction through an adaptive structure that dynamically adjusts the importance of each control objective in real time. The proposed structure consists of SMO, UKF, and adaptive weight calculations and does not require an iterative optimization process. Therefore, computational complexity is primarily determined by the sigma point update process of the UKF, and the adaptive weight calculation consists of simple algebraic operations, resulting in minimal additional computational burden. Due to these characteristics, the proposed method is expected to have a computational complexity suitable for application in real-time wind turbine control systems.

4.2. Fatigue load-aware adaptive torque controller stability verification

Theorem:

The proposed torque controller is defined in (63), and the wind turbine dynamics are given in (10). Under the following assumptions, the closed-loop system state ω is uniformly ultimately bounded (UUB).

Assumptions:

A1. The aerodynamic torque is bounded, i.e., $|T_a(t)| \leq T_a^{max}$.

A2. All weighting factors are positive and bounded.

A3. The DEL estimate and torque rate of change are bounded.

Proof:

T_e^* is constructed as a weighted sum as in (64), and since all weighting factors are strictly positive and normalized by their sum, it takes the form of a convex combination. Therefore, the control input does not exceed the range of each component, and its upper bound is determined as in (70). Here, $\hat{T}_a$ is physically bounded, $T_{e,target}$ can be considered bounded as it is limited within the physical operating range of the system, and $T_e^*(k-1)$ is also bounded as it represents the previous control input. Thus, the control input T_e^* is always bounded, and consequently, condition (71) is satisfied.

$$|T_e^*| \leq max\{T_{e,target}, |\hat{T}_a|, |T_e^*(k-1)|\} \tag{70}$$

$$|T_e^*| \leq T_e^{max}. \tag{71}$$

The Lyapunov candidate function and its derivative are defined as follows [43]:

$$V_2 = \frac{1}{2}{\omega_m}^2 \tag{72}$$

$$\dot{V}_2 = \omega_m \dot{\omega}_m = \frac{\omega_m}{J}(T_a - T_e - B\omega_m). \tag{73}$$

Using Assumption A1 and (71), (74) can be obtained.

$$\dot{V}_2 \leq \frac{|\omega_m|}{J}(T_a^{max} + T_e^{max}) - \frac{B}{J}{\omega_m}^2 \rightarrow \dot{V}_2 \leq -c_1{\omega_m}^2 + c_2|\omega_m|. \tag{74}$$

Here, $c_1 = \frac{B}{J}$, and $c_2 = \frac{(T_a^{max}+T_e^{max})}{J}$. Therefore, when (76) holds, $\dot{V}_2 < 0$, and the system state is stable.

$$|\omega_m| > \frac{T_a^{max}+T_e^{max}}{B} \implies \dot{V}_2 < 0 \tag{76}$$

$$|\omega_m| \leq \frac{T_a^{max}+T_e^{max}}{B}. \tag{77}$$

This means that, even in the presence of disturbances, the state converges to a finite region around the origin and remains within that region after sufficient time has elapsed. Consequently, the system satisfies the UUB property. Consequently, in the proposed SMO-UKF-based fatigue-sensitive adaptive torque control framework, the SMO-UKF estimator guarantees a uniformly ultimately bounded estimation error under bounded disturbances, ensuring that all estimation states used in the control law are bounded. Furthermore, the proposed adaptive controller is designed as a continuous function of these bounded estimates and bounded auxiliary signals, such as torque change and fatigue index, so the control input is also uniformly bounded. Substituting the bounded control input and the bounded disturbance term into the rotational velocity dynamics reveals that the closed-loop system can be represented as a system driven by bounded inputs. Based on the serial connection structure and standard Lyapunov-based results for cascade systems and input-to-state boundedness properties, all closed-loop signals maintain a uniformly ultimately bounded state.

5. Simulation

In this section, simulations were conducted on a PMSG-based wind turbine system to verify the performance of the proposed SMO-UKF estimator and the fatigue load-aware adaptive torque controller. The overall system was modeled in MATLAB/Simulink 2024a with an ode3 solver with a sampling time of 0.001 Ts. The simulation target system consists of a 1.5 MW wind turbine, based on an integrated model that includes aerodynamics, drivetrain, and generator dynamics. The main system parameters were set with reference to [40]. The parameters of the wind turbine system, estimator, and controller are presented in Table 1.

To verify the effectiveness and robustness of the proposed estimator and controller, three turbulent wind speed scenarios with distinct characteristics were applied, as shown in Figure 5. The wind profile is generated by combining time-varying wind speed with turbulence and small oscillatory components containing multiple frequency components. The turbulence intensities of the wind scenarios account for (a) 5.7%, (b) 12.9%, and (c) 15%. In particular, the profiles are designed to include wind speed ramp-up, steady-state, and rapid change events to emulate various real-world operating conditions. All simulations are carried in the Region 2 of wind turbine operation for 1400 s.

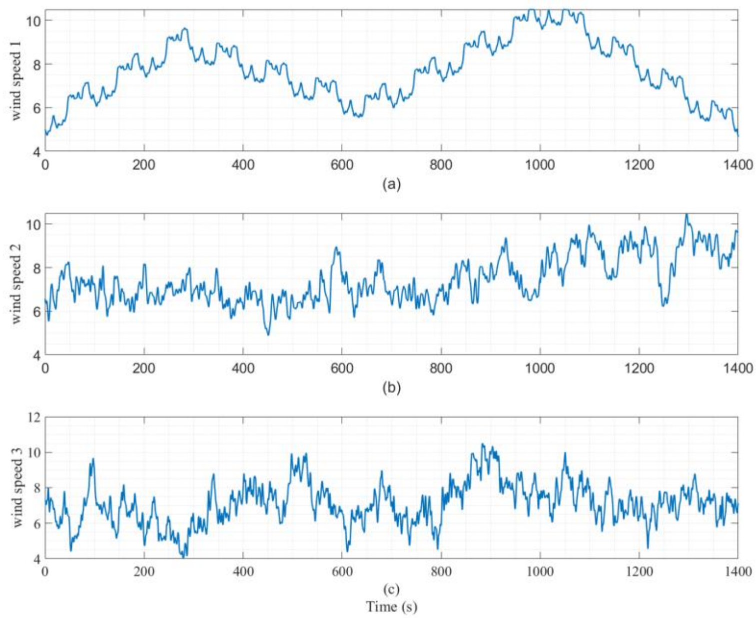

Figure 5. Wind speed scenarios: (a) turbulence intensity 5.7%, (b) turbulence intensity 12.9%, (c) turbulence intensity 15%.

Table 1. System parameters.

Parameter	Description	Value
	WTS parameters	
$P_{rated}(MW)$	Rated power	1.5
$\rho(kg/m^3)$	Air density	1.225
$R_B(m)$	Blade radius	35.25
λ_{opt}	Optimal tip speed ratio	8.1
C_p^{max}	Maximum power coefficient	0.48
$v_{cut-in}(m/s)$	Cut-in wind speed	3
$v_{rated}(m/s)$	Rated wind speed	11
	PMSG parameters	
$J(MNm)$	Total inertia	4.872
$\psi_{mag}(Wb)$	Generator air-gap flux	7.0172
p_g	Generator pole pairs	402
$R_p(m\Omega)$	Stator resistance	3.17
L_d, $L_q(mH)$	Inductances	3.7
	SMO-UKF estimation parameters	
α_{T_a}	1-st LPF weight	1.0
p	Nonlinear exponent of the sliding surface	0.9
k_1	SMO gain	3.5
k_2	SMO gain	1.0
ϕ	SMO boundary layer	1.0
α_u	Sigma point parameter	1×10^{-3}
β_u	Sigma point parameter	2.0
κ_u	Sigma point parameter	0
Q_ω	Rotor speed process noise variances	9×10^{-4}
Q_{T_a}	Aerodynamic torque process noise variances	5×10^{9}
R	Measurement noise variance	1×10^{-10}
	Fatigue load-aware adaptive torque controller	
K_{opt}	Optimal torque constant	94,588.37
N_{hist}	History window length	100
$\alpha_{1,aero}$	Controller design parameter	0.4
$\alpha_{2,aero}$	Controller design parameter	0.2
$\alpha_{1,damp}$	Controller design parameter	40
$\alpha_{2,damp}$	Controller design parameter	20
$\alpha_{1,mppt}$	Controller design parameter	1.3
$\alpha_{2,mppt}$	Controller design parameter	1.5
T_e^{max}	Generator torque maximum	1.5×10^{6}

In all simulations, uncertainties and noise were considered to realistically reflect practical operating conditions. First, white Gaussian noise was added to the rotor speed to emulate sensor noise, thereby incorporating measurement uncertainty. In addition, to account for parameter uncertainty, variations within a certain range (±20%) were applied to the inertia and viscous damping coefficients to represent modeling errors and parameter uncertainties. High-frequency torque ripple (approximately 2%) was also included in the generator torque to reflect switching effects in the power converter. This high-frequency component is an inherent characteristic of real power electronic systems and serves as an important factor in evaluating controller robustness. By conducting simulations under these noise- and uncertainty-inclusive conditions, the practical applicability and robustness of the proposed estimator and controller were comprehensively validated.

5.1. SMO-UKF estimation simulation

The key parameters of the proposed SMO-UKF estimator were empirically determined through iterative experiments in a simulation environment and are shown in Table 1. The gains k_1 and k_2 of the SMO directly affect the convergence speed of the estimation error and the disturbance suppression performance. While increasing the gain allows for faster convergence characteristics, it may increase chatter; therefore, the values were selected considering estimation stability. The boundary layer ϕ was adjusted to mitigate chatter and was set to prevent a decrease in estimation accuracy caused by excessive boundary layer settings. Additionally, the process noise covariance of the UKF was set as Q_ω and Q_{T_a} for the rotor speed and aerodynamic torque states, respectively. Q_ω affects the estimation performance regarding dynamic changes in the rotor speed state; while increasing the value improves sensitivity to state changes, it may increase estimation variability. On the other hand, Q_{T_a} affects the response characteristics of aerodynamic torque estimation and was set to appropriately reflect aerodynamic torque fluctuations caused by turbulence. The measurement noise covariance R was selected considering the measurement noise level and adjusted to ensure a balance between estimation responsiveness and noise robustness. The sigma point parameter was set considering the approximation accuracy and numerical stability of the state distribution.

The proposed SMO-UKF estimator is structured as a combination of SMO and UKF, and its key parameters were empirically determined through iterative experiments in the simulation environment. In particular, the SMO gains and boundary layer parameter, as well as the covariance matrices of the UKF, were tuned by considering the trade-off between estimation error and convergence speed, while also minimizing chattering. To validate the performance of the proposed estimator, the estimated aerodynamic torque and rotor speed were compared with their actual values. Furthermore, a quantitative analysis of the estimation performance of the proposed SMO-UKF was conducted by comparing it with SMO-DOB, SMO-EKF, and UKF estimators. In addition, for a fair quantitative evaluation, the conventional OTC method was applied in Region 2 operation, and the results were used as a baseline for comparison.

5.1.1. Simulation test case 1

Initially, the performance of the proposed SMO-UKF estimator was evaluated under a turbulence intensity of 5.7%. The corresponding wind speed profile is shown in Figure 5(a), and the overall simulation results are presented in Figure 6. Figure 6(a) shows the rotor speed ω_m estimation results, while Figure 6(b) presents the corresponding estimation errors. Figure 6(c),(d) illustrates the aerodynamic torque estimation $\hat{T}_a$ results and their estimation errors, respectively. In each figure, the performance of the proposed SMO-UKF is compared with that of SMO-DOB, SMO-EKF, UKF, and ST-SMO estimators. From Figure 6(a), it can be observed that the conventional UKF is sensitive to the setting of the measurement noise covariance, resulting in relatively large estimation errors. In contrast, the proposed SMO-UKF obtains noise-suppressed rotor speed through SMO-based estimation. Furthermore, in Figure 6(c), the conventional ST-SMO still exhibits some chattering effects, whereas the proposed SMO-UKF effectively suppresses them, providing smoother aerodynamic torque estimation $\hat{T}_a$ results. The quantitative comparison results are summarized in Table 2. Compared to SMO-EKF, the proposed estimator improves the RMSE of rotor speed estimation by 18.15% and the RMSE of aerodynamic torque estimation by 2.77%. Therefore, it is confirmed that the proposed SMO-UKF estimation method provides stable and accurate estimation performance under the 5.7% turbulence condition.

Table 2. Estimator simulation result.

		SMC-DOB	SMO-UKF	SMO-EKF	UKF	ST_SMO
Simulation 1	$\hat{T}_a$ RMSE	34890.906	30701.455	31576.705	34582.731	42467.693
	$\hat{T}_a$ NRMSE	0.107589	0.094675	0.097369	0.106638	0.130952
	$\hat{T}_a$ Corr	0.948487	0.962295	0.96016	0.953544	0.927273
	$\hat{T}_a$ Delay	4.667	1.404	1.722	1.639	2.32
	$\hat{\omega}$ RMSE	0.014424	0.011839	0.014465	0.031551	0.011719
	$\hat{\omega}$ NRMSE	0.008044	0.006602	0.008067	0.017595	0.006535
	$\hat{\omega}$ Corr	0.998895	0.999255	0.998889	0.994746	0.999271
	$\hat{\omega}$ Delay	0	0	0	0	0
Simulation 2	$\hat{T}_a$ RMSE	57649.533	43096.906	44129.07588	46317.0135	56235.9145
	$\hat{T}_a$ NRMSE	0.196615	0.146983	0.150503	0.157965	0.191794
	$\hat{T}_a$ Corr	0.851349	0.922871	0.918701	0.914918	0.864314
	$\hat{T}_a$ Delay	4.536	1.708	1.724	1.635	2.601
	$\hat{\omega}$ RMSE	0.014575	0.012036	0.014448	0.031551	0.011854
	$\hat{\omega}$ NRMSE	0.008648	0.007141	0.008573	0.01872	0.007033
	$\hat{\omega}$ Corr	0.998714	0.999124	0.998737	0.994015	0.99915
	$\hat{\omega}$ Delay	0	0	0	0	0
Simulation 3	$\hat{T}_a$ RMSE	65076.349	48748.610	50029.818	53596.498	61443.829
	$\hat{T}_a$ NRMSE	0.236916	0.177474	0.182138	0.195123	0.223692
	$\hat{T}_a$ Corr	0.746828	0.873772	0.865985	0.856734	0.788421
	$\hat{T}_a$ Delay	5.282	1.682	1.674	1.696	2.6
	$\hat{\omega}$ RMSE	0.014653	0.012268	0.014618	0.031551	0.01219
	$\hat{\omega}$ NRMSE	0.008891	0.007444	0.00887	0.019144	0.007397
	$\hat{\omega}$ Corr	0.997828	0.998483	0.997841	0.990039	0.998499
	$\hat{\omega}$ Delay	0.267	0.201	0.151	0.066	0.221

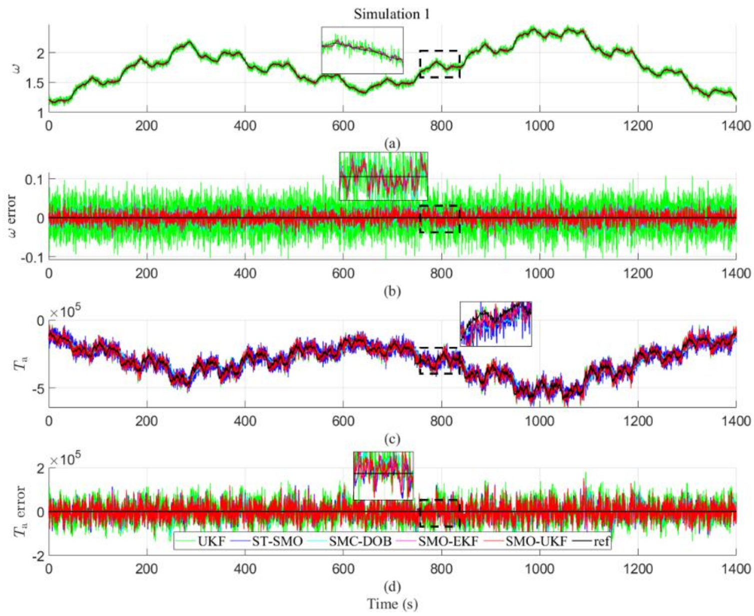

Figure 6. Simulation 1: (a) $\boldsymbol{\omega_m}$ estimation result, (b) $\boldsymbol{\omega_m}$ estimation error, (c) $\boldsymbol{\hat{T}_a}$ result, (d) $\boldsymbol{\hat{T}_a}$ error.

5.1.2. Simulation test case 2

Next, to verify the performance and robustness of the proposed estimator, simulations were conducted under a different wind speed profile with a turbulence intensity of 12.9%. The wind speed profile is shown in Figure 5(b), representing a more severe operating condition compared to the 5.7% turbulence case. The results of Simulation 2 are presented in Figure 7, where Figure 7(a)–(d) illustrates the rotor speed ω_m estimation results, rotor speed ω_m estimation errors, aerodynamic torque estimation $\hat{T}_a$ results, and their corresponding errors, respectively. From Figure 7(a),(b), it can be observed that the conventional UKF exhibits a large error range due to disturbances, whereas the proposed SMO-UKF demonstrates robust rotor speed estimation against disturbances through the SMO. Furthermore, as shown in Figure 7(c),(d), the conventional ST-SMO, SMC-DOB, and UKF all produce significant estimation errors during rapid changes in aerodynamic torque. In contrast, the proposed SMO-UKF maintains fast response and low estimation error despite abrupt disturbance variations. This can be interpreted as the SMO effectively filtering disturbance and noise components in advance, allowing the UKF to perform accurate state estimation based on the refined input. The quantitative results are summarized in Table 2, where the proposed SMO-UKF improves the RMSE of aerodynamic torque estimation by 2.34% and the RMSE of rotor speed estimation by 16.7% compared to SMO-EKF. These results demonstrate that the proposed SMO-UKF method does not rely on a specific wind speed pattern and can maintain stable and consistent estimation performance under various disturbance conditions.

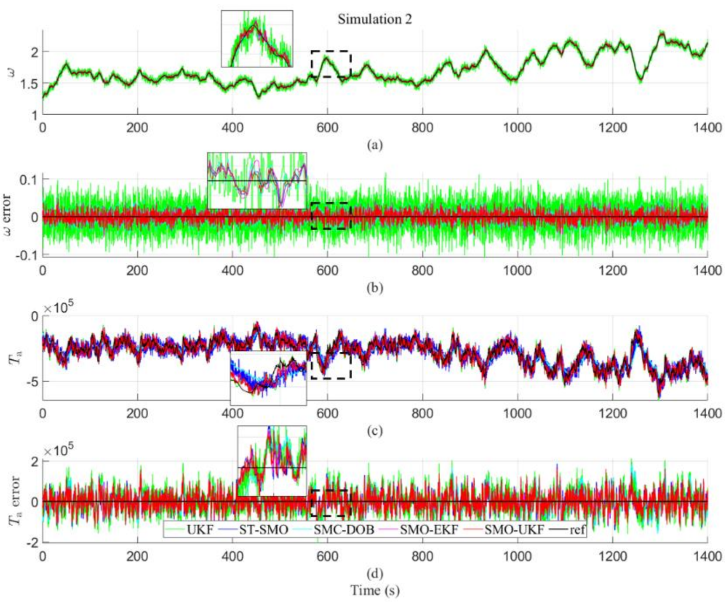

Figure 7. Simulation 2: (a) $\boldsymbol{\omega_m}$ estimation result, (b) $\boldsymbol{\omega_m}$ estimation error, (c) $\boldsymbol{\hat{T}_a}$ result, (d) $\boldsymbol{\hat{T}_a}$ error.

5.1.3. Simulation test case 3

To evaluate the generalization performance of the estimator under varying input conditions and its robustness against increased disturbances, a wind speed profile with a turbulence intensity of 15%, different from the previous scenarios, was applied. The wind speed profile is presented in Figure 5(c), and the results of Simulation 3 are shown in Figure 8. Figure 8(a)–(d) illustrates the rotor speed ω_m estimation results and their corresponding errors, as well as the aerodynamic torque estimation $\hat{T}_a$ results and their errors, respectively. As observed in Figure 8(a),(b), the conventional UKF exhibits a large error range due to the effects of turbulence and disturbances. In contrast, ST-SMO, SMC-DOB, SMO-EKF, and the proposed SMO-UKF demonstrate robust rotor speed ω_m estimation performance against disturbances owing to their sliding mode-based characteristics. Meanwhile, as shown in Figure 8(c),(d), ST-SMO and UKF exhibit relatively large error ranges in aerodynamic torque estimation $\hat{T}_a$, and SMC-DOB shows a noticeable delay. On the other hand, the proposed SMO-UKF estimates the aerodynamic torque in the UKF based on the rotor speed ω_m estimated by the SMO, resulting in a small error range and fast response despite disturbances and turbulence. Quantitatively, the proposed SMO-UKF improves the RMSE of aerodynamic torque estimation $\hat{T}_a$ by 2.56% and the RMSE of rotor speed ω_m estimation by 16.08% compared to SMO-EKF, as summarized in Table 2. These results confirm that the proposed SMO-UKF method can provide effective estimation even under severe turbulence and disturbance conditions.

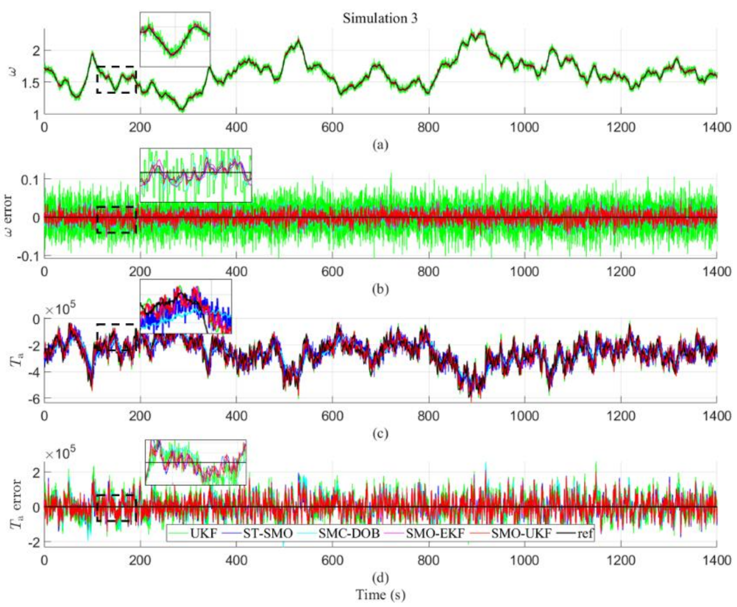

Figure 8. Simulation 3: (a) $\boldsymbol{\omega_m}$ estimation result, (b) $\boldsymbol{\omega_m}$ estimation error, (c) $\widehat{\boldsymbol{T}}_{\boldsymbol{a}}$ result, (d) $\widehat{\boldsymbol{T}}_{\boldsymbol{a}}$ error.

The results of the three simulations demonstrate that the proposed SMO-UKF estimator robustly estimates aerodynamic torque under turbulent wind speed conditions. Even in the presence of measurement noise and parameter uncertainty, the estimation error remains small throughout the simulation period. This is because SMO effectively suppresses disturbances in the rotational speed signal, and UKF utilizes filtered information to precisely estimate nonlinear aerodynamic torque dynamics. Consequently, the proposed estimator achieves improved estimation accuracy and robustness compared to existing benchmark techniques. This validity is clearly supported by Table 2. As shown in Table 2, the proposed SMO-UKF consistently recorded the lowest RMSE and NRMSE for all turbulent scenarios. This demonstrates excellent state estimation performance even under harsh turbulent operating conditions.

In this study, simulations were conducted considering sensor noise and parameter uncertainties to reflect realistic wind turbine operating conditions. Modeling uncertainties were incorporated by applying ±20% variations to the inertia and viscous damping coefficients. In addition, Gaussian noise was added to the sensor measurements, and high-frequency ripple was included in the generator torque signal. The proposed SMO–UKF estimator employs a cascaded structure that combines SMO-based disturbance and noise rejection with UKF-based nonlinear state estimation, thereby providing a certain degree of robustness against measurement noise and modeling errors. Accordingly, the proposed estimator demonstrated stable estimation performance under the uncertainty conditions considered in this study. However, if the level of uncertainty increases significantly beyond the considered range, or if severe sensor degradation or sensor failures occur, the estimation accuracy may gradually deteriorate. This behavior is generally observed in model-based observer structures.

5.2. Fatigue load-aware adaptive torque controller simulation

The proposed controller generates a final torque command by adaptively adjusting weights based on the aerodynamic torque estimate, the rate of change of torque, and the fatigue load index. In the proposed controller, $\alpha_{1,aero}$, $\alpha_{2,aero}$, $\alpha_{1,damp}$, and $\alpha_{2,damp}$ are adaptive weight adjustment parameters that determine the degree of weight change according to the mismatch between the aerodynamic torque and the generator torque δ_{mis} and the rate of change of aerodynamic torque ΔT_a. It is designed so that w_{aero} increases and w_{damp} decreases when δ_{mis} or ΔT_a increases, and each parameter determines the sensitivity of this weight redistribution. Additionally, $\alpha_{1,mppt}$ and $\alpha_{2,mppt}$ are parameters that determine the change characteristics of the MPPT weight w_{mppt}. $\alpha_{1,mppt}$ determines the degree of reduction in the MPPT weighting for the torque fluctuation index T^*_{fluc}; as the value increases, the MPPT tracking weighting decreases more rapidly in situations with large torque fluctuations, thereby enhancing the fatigue load reduction effect. On the other hand, $\alpha_{2,mppt}$ determines the degree of increase in the MPPT weighting according to the aerodynamic torque change rate $|\Delta T_a|$ and plays a role in adjusting the power generation performance so that it does not degrade excessively even under conditions of large wind speed changes. As each parameter value increases, weighting adjustments are performed more actively in response to changes in operating conditions, and the controller's adaptability to changes in aerodynamic torque is improved. However, since excessive parameter settings can increase weighting variability and cause unnecessary vibrations in the control input, the final values were selected by considering the balance between power generation performance and torque fluctuation suppression performance, and are presented in Table 1.

The proposed controller aims to reduce torque fluctuations and fatigue loads while maintaining MPPT performance. To evaluate the performance of the proposed controller, we compare it with the performance of the OTC technique and OTC-LFP, which are widely used in the field of wind torque control [20]. In addition, to analyze the contribution of each component of the proposed controller, two additional cases are considered: one without the adaptive mechanism and another with reduced weighting components. Fixed-3W represents the case where the weights are fixed as constant values without time-varying updates, effectively removing the adaptive mechanism. Fixed-2W represents the case where $\boldsymbol{w_{damp}}$ is removed. Through this, the structural validity of the proposed controller and the contribution of each component were quantitatively evaluated. In particular, the ablation study enables the individual analysis of the adaptive weighting mechanism and the impact of each control component on power generation performance and fatigue load reduction, thereby more clearly identifying the causes of the performance improvement of the proposed controller.

The performance of the proposed controller is evaluated in terms of power capture efficiency and fatigue load reduction. The evaluation metrics include the average power coefficient $\boldsymbol{C_p}$, the standard deviation and rate of change of generator torque, and the DEL based on generator torque. In a DD-PMSG structure, the generator is directly coupled to the rotor without a gearbox, meaning that the generator torque is directly transmitted through the drivetrain. Therefore, when torsional dynamics are neglected or low-frequency behavior is considered, the generator torque can be used as an approximate indicator of shaft torque. In this study, the DEL is calculated based on load cycles extracted using the Rainflow counting method, combined with Miner's rule and S-N curves. To analyze fatigue sensitivity to load variations, the Wohler exponent m is set to 4, 6, and 8. In general, a larger m value implies higher sensitivity to large load cycles; therefore, analyzing multiple m values allows for a more comprehensive evaluation of the fatigue reduction performance of the proposed controller [5,45]. DEL is an indicator that represents the cumulative fatigue damage caused by a given load history as a single equivalent load and is widely used to quantitatively compare the effects of fatigue loads between different control strategies [5,45].

5.2.1. Simulation 1

To evaluate the performance of the designed controller, simulations were conducted under a turbulence intensity of 5.7%. The corresponding wind speed profile is shown in Figure 5(a), and the overall simulation results are presented in Figure 9. Figure 9(a) shows the generator torque $\boldsymbol{T_e}$, where the proposed method effectively suppresses torque fluctuations and peak values. Figure 9(b) presents the rotor speed $\boldsymbol{\omega_m}$, demonstrating that it is maintained stably without unstable behavior during the control process. Figure 9(c),(d) illustrates the generator power $\boldsymbol{P_e}$ and aerodynamic power $\boldsymbol{P_a}$, respectively, which are maintained at levels nearly identical to those of conventional methods. In Figure 9(e), the power coefficient $\boldsymbol{C_p}$ shows slight reductions in certain intervals; however, this is a result of control actions aimed at load mitigation. Quantitatively, compared to the conventional OTC method, the proposed control approach results in reductions of 0.69% in generator power $\boldsymbol{P_e}$, 1.68% in aerodynamic power $\boldsymbol{P_a}$, and 1.53% in average $\boldsymbol{C_p}$. However, the energy conversion efficiency is improved by 0.7%, while the torque standard deviation is reduced by 13.53%, and the DEL (m = 6) is reduced by 15.52%. This indicates that the proposed method achieves more than a 15% reduction in DEL while incurring less than a 1% loss in output power, demonstrating an effective trade-off between power performance and load mitigation. The quantitative comparison results are summarized in Table 3. These results confirm that the proposed control method provides stable control performance and meaningful fatigue load reduction under a turbulence intensity of 5.7%.

Table 3. Controller simulation results.

		OTC	OTC-LPF	Fixed-2W	Fixed-3W	Proposed
Simulation 1	Average $\boldsymbol{C_p}$	0.4767	0.4769	0.4752	0.4767	0.4694
	$\boldsymbol{P_e}$	210.68	210.75	210.85	210.68	208.7893
	$\boldsymbol{P_a}$	221.92	222.00	221.41	221.92	218.299
	$\boldsymbol{P_e/P_a}$	94.94	94.93	95.23	94.93	95.64
	standard deviation	104608.79	104765.53	101113.90	104603.32	90451.37
	DEL(m=4)	74869.03	73985.75	72071.02	74493.87	63345.68
	DEL(m=6)	131981.70	130349.50	127059.33	131296.26	111486.83
	DEL(m=8)	176554.64	174279.26	169962.91	175590.51	148977.90
Simulation 2	Average $\boldsymbol{C_p}$	0.4732	0.4734	0.4717	0.4732	0.4664
	$\boldsymbol{P_e}$	183.55	183.61	183.78	183.54	182.25
	$\boldsymbol{P_a}$	194.40	194.50	194.21	194.40	192.23
	$\boldsymbol{P_e/P_a}$	94.42	94.4	94.63	94.41	94.81
	standard deviation	74413.54	74793.26	72026.84	74412.57	65100.66
	DEL(m=4)	57448.26	58228.65	55519.16	57130.15	51784.53
	DEL(m=6)	98332.61	100021.31	95502.77	97949.07	88887.02
	DEL(m=8)	132876.56	135408.14	129310.05	132442.07	120516.38
Simulation 3	Average $\boldsymbol{C_p}$	0.4659	0.4663	0.4634	0.4659	0.4575
	$\boldsymbol{P_e}$	161.891	162.0177	162.2958	161.8903	161.3823
	$\boldsymbol{P_a}$	169.08	169.2214	169.0092	169.086	167.4679
	$\boldsymbol{P_e/P_a}$	95.75	95.74	96.03	95.74	96.37
	standard deviation	70837.06	71424.95	68630.7	70844.76	62713.93
	DEL(m=4)	70296.7	69649.762	67347.66	70212.32	62228.55
	DEL(m=6)	118631.04	116867.56	113665.73	118564.67	104466.96
	DEL(m=8)	157076.07	154312.21	150515.46	157004.63	138194.95

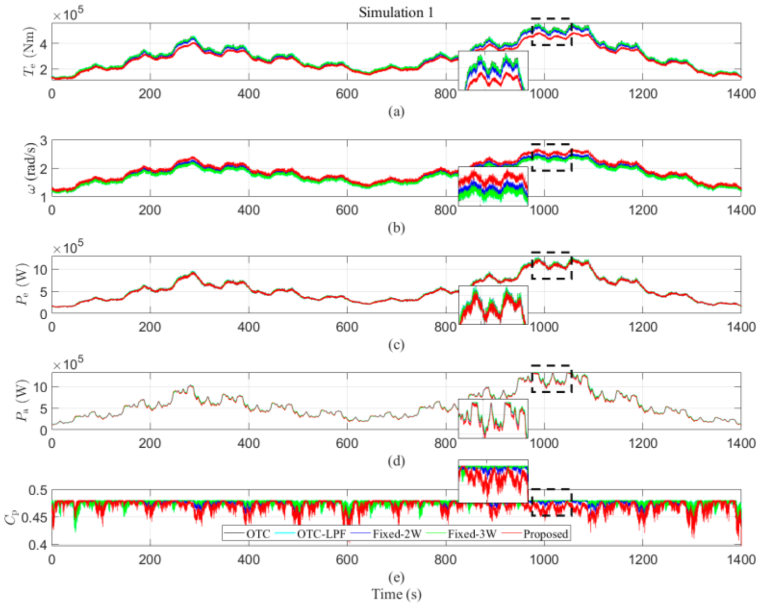

Figure 9. Simulation 1: (a) generator torque $\boldsymbol{T_e}$, (b) rotor speed $\boldsymbol{\omega_m}$, (c) generator power $\boldsymbol{P_e}$, (d) aerodynamic power $\boldsymbol{P_a}$, (e) power coefficient $\boldsymbol{C_p}$.

5.2.2. Simulation 2

To evaluate the applicability of the designed controller under various operating conditions, simulations were conducted under a turbulence intensity of 12.9%. The wind speed profile is shown in Figure 5(b), and the overall results are presented in Figure 10. Figure 10(a) shows the generator torque $\boldsymbol{T_e}$. As turbulence intensity increases, conventional methods exhibit larger torque fluctuations and peaks, whereas the proposed method effectively suppresses these variations. Figure 10(b) shows the rotor speed $\boldsymbol{\omega_m}$, confirming stable operation even under increased fluctuations. Figure 10(c),(d) presents the generator power $\boldsymbol{P_e}$ and aerodynamic power $\boldsymbol{P_a}$, respectively, which remain at levels comparable to those of conventional methods, indicating no significant degradation in power performance. In Figure 10(e), the power coefficient $\boldsymbol{C_p}$ shows slight reductions in certain intervals; however, this can be interpreted as a result of control actions aimed at mitigating increased loads. Quantitatively, the proposed method shows slight decreases of 0.71% in generator power $\boldsymbol{P_e}$ and 1.44% in average $\boldsymbol{C_p}$, while achieving reductions of 9.61% in DEL (m = 6) and 12.51% in torque standard deviation. The overall quantitative results are summarized in Table 3, confirming that the proposed method effectively reduces torque fluctuations and DEL without significant loss in power performance. Notably, the load reduction performance is maintained even under increased turbulence intensity, indicating that the proposed control method operates reliably under harsh operating conditions.

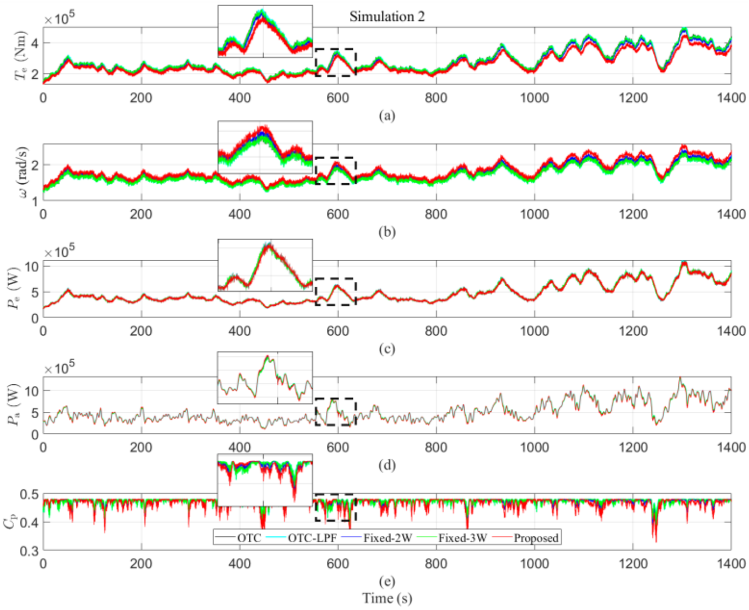

Figure 10. Simulation 2: (a) generator torque $\boldsymbol{T_e}$, (b) rotor speed $\boldsymbol{\omega_m}$, (c) generator power $\boldsymbol{P_e}$, (d) aerodynamic power $\boldsymbol{P_a}$, (e) power coefficient $\boldsymbol{C_p}$.

5.2.3. Simulation 3

To evaluate the performance of the proposed control method under extreme conditions, simulations were conducted with more aggressive wind profiles and a turbulence intensity of 15%. The wind speed profile is shown in Figure 5(c), and the overall results are presented in Figure 11. Figure 11(a) shows the generator torque $\boldsymbol{T_e}$. Under high turbulence conditions, conventional control methods exhibit large-amplitude torque fluctuations and peaks, whereas the proposed method effectively mitigates these variations. Figure 11(b) presents the rotor speed $\boldsymbol{\omega_m}$, which remains stable despite increased fluctuations, confirming the stability of the control system. Figure 11(c),(d) shows the generator power $\boldsymbol{P_e}$ and aerodynamic power $\boldsymbol{P_a}$, respectively, which remain comparable to those of conventional methods, demonstrating that power performance is maintained even under extreme conditions. In Figure 11(e), the power coefficient $\boldsymbol{C_p}$ decreases in some intervals; however, this can be interpreted as a result of control actions aimed at alleviating increased loads. Quantitatively, compared to the conventional OTC method, the proposed method shows slight reductions of 0.31% generator power $\boldsymbol{P_e}$ and 1.8% in average $\boldsymbol{C_p}$. However, it achieves reductions of 11.94% in DEL (m = 6) and 11.47% in torque standard deviation, confirming that fatigue loads are effectively reduced without significant power loss. The overall results are summarized in Table 3, demonstrating that the load reduction performance is maintained even under high turbulence conditions and that the proposed control method operates reliably under extreme operating conditions.

Simulation results of torque control for fatigue load reduction under three turbulent conditions showed that the proposed method effectively suppresses generator torque fluctuations caused by turbulence, smoothing drivetrain dynamics, and mitigating rotational speed variations compared to conventional methods. It was confirmed that MPPT performance is maintained, with $\boldsymbol{C_p}$ remaining near the optimal region. Collectively, these results demonstrate that the proposed method achieves stable closed-loop operation under turbulent wind speed conditions by mitigating torque fluctuations and ensuring consistent energy conversion performance.

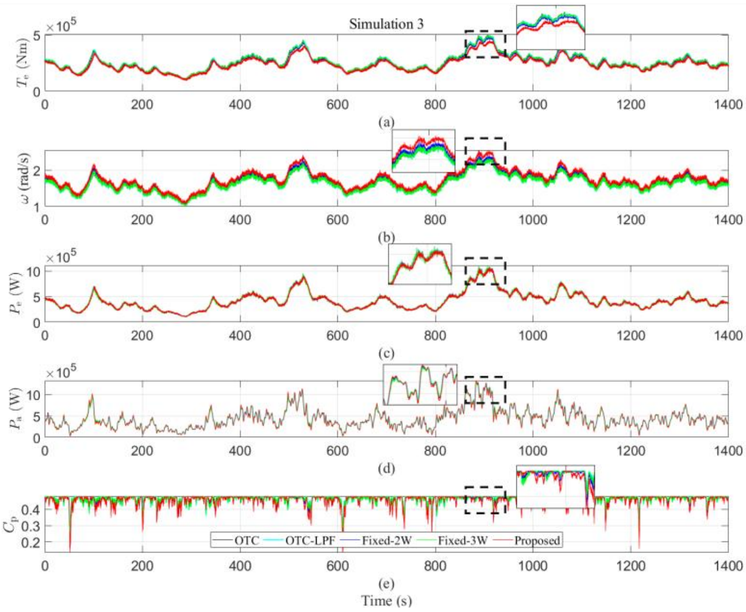

Figure 11. Simulation 3: (a) generator torque $\boldsymbol{T_e}$, (b) rotor speed $\boldsymbol{\omega_m}$, (c) generator power $\boldsymbol{P_e}$, (d) aerodynamic power $\boldsymbol{P_a}$, (e) power coefficient $\boldsymbol{C_p}$.

Figure 12 presents a trade-off graph comparing the relationship between output performance and DEL for the proposed method and conventional control methods under three turbulent wind simulations, along with the DEL results for each simulation and different Wohler exponent m. The x-axis represents the generator power $\boldsymbol{P_e}$, and the y-axis represents the DEL corresponding to the generator torque. Each scenario is distinguished by different markers, while each control method is indicated by different colors. From Figure 12(a)–(c), it can be observed that the proposed control method effectively reduces DEL while causing almost no loss in generator power $\boldsymbol{P_e}$ compared to conventional methods. This demonstrates that the proposed approach alleviates the trade-off between output performance and fatigue load while simultaneously improving overall performance. Furthermore, as shown in Figure 12(d)–(f), the proposed method consistently achieves the lowest DEL across various simulation conditions with different Wohler exponents and turbulence intensities. A decrease in DEL means that the rate of cumulative fatigue damage decreases in terms of Miner's linear damage rule, and assuming the same operating conditions continue, it indicates the possibility of an increase in the relative fatigue life of the drivetrain components. In other words, the proposed control method can be interpreted as working to lower the rate of fatigue damage accumulation by mitigating load fluctuations [5,45]. These results indicate that the proposed control method maintains robust performance under diverse operating conditions. Furthermore, the results of the ablation study showed that Fixed-3W exhibited greater torque fluctuation and DEL compared to Fixed-2W. This demonstrates that the adaptive mechanism, which adjusts control weights in real-time according to operating conditions, contributes to the reduction of fatigue load. Meanwhile, although Fixed-2W showed some improved performance compared to Fixed-3W, the proposed method achieved the lowest torque fluctuation and DEL. These results indicate that the adaptive weight structure and the damping weight term work complementarily to effectively reduce fatigue load without a significant degradation in power generation performance.

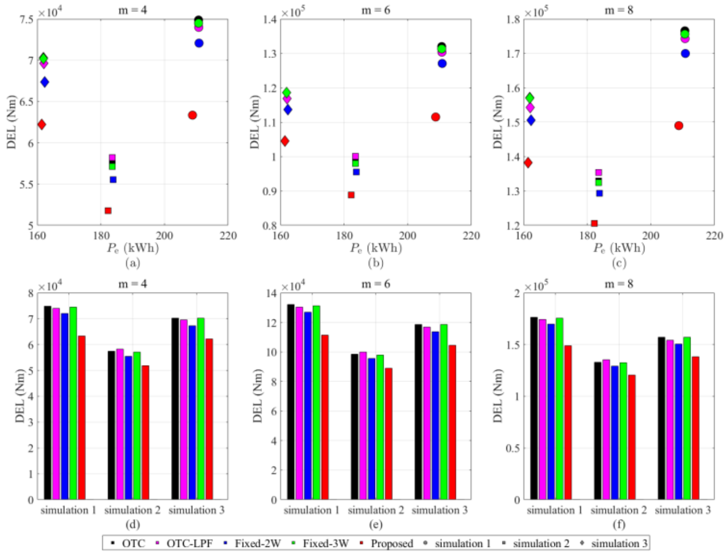

Figure 12. P_e-DEL trade-off and DEL values for different Wohler exponents.

5.3. State estimation and stabilization analysis

To verify the performance of the proposed SMO-UKF estimator, additional state estimation analysis was performed under constant conditions of a wind speed of 8 m/s. Figure 13 shows the state estimation performance of the SMO-UKF estimator. Figure 13(a) shows the wind speed, Figure 13(b) shows the estimated aerodynamic torque, and Figure 13(c) shows the error. As shown in Figure 13, the estimated aerodynamic torque closely follows the actual aerodynamic torque after a short transient period. The estimation error initially exhibits a large deviation due to initialization conditions; however, it rapidly converges to zero and remains negligible in the steady state. These results demonstrate the convergence, accuracy, and stability of the proposed estimator under steady operating conditions. The absence of steady-state estimation error confirms that the proposed SMO-UKF scheme can provide reliable aerodynamic torque information for the fatigue load-aware adaptive torque control system, thereby contributing to stable turbine operation and improved control performance.

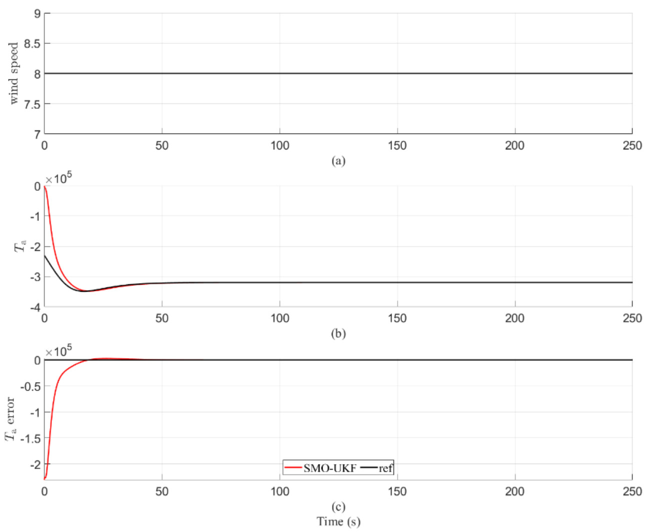

Figure 13. State estimation performance of the proposed SMO-UKF estimator.

Figure 14 presents the stabilization performance of the proposed fatigue load-aware adaptive torque control strategy under a constant wind speed condition. Figure 14(a) shows the wind speed. As shown in Figure 14(b), the proposed controller achieves a smooth and stable electromagnetic torque response, converging to a lower steady-state torque level than the conventional optimal torque control (OTC) strategy. This reduction in torque demand contributes to mitigating mechanical stress and fatigue loading on the drivetrain components. Furthermore, Figure 14(c) shows that the power coefficient remains close to its maximum value despite the reduced torque command. Specifically, the proposed controller maintains a steady-state power coefficient of approximately 0.473, compared to 0.48 obtained by the OTC strategy, corresponding to only a marginal reduction of approximately 1.4%. These results indicate that the proposed method successfully achieves a favorable trade-off between load alleviation and energy capture, maintaining near-optimal aerodynamic efficiency while enhancing the overall stability of the wind energy conversion system.

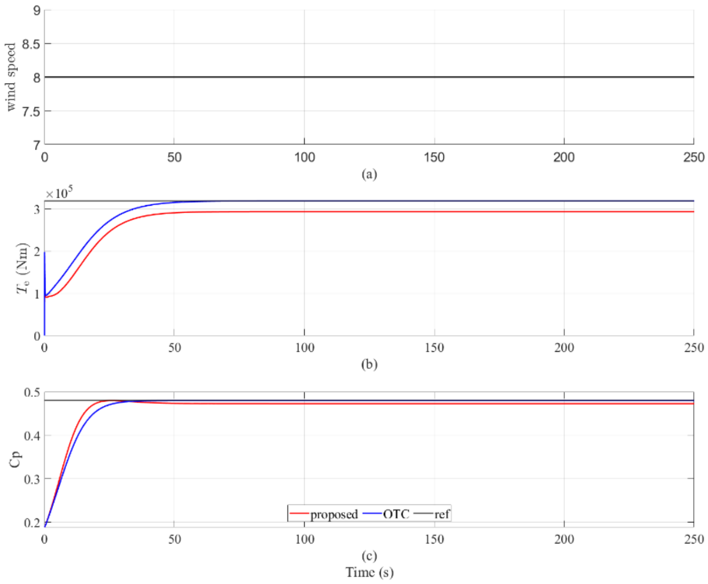

Figure 14. Stabilization characteristics of the proposed fatigue load-aware adaptive torque control.

6. Conclusions

In this study, we proposed an SMO-UKF-based estimator and a fatigue-aware adaptive torque control technique capable of effectively reducing fatigue loads on generator drive systems and minimizing power generation efficiency degradation in wind power environments characterized by extreme turbulence, sensor noise, and parameter uncertainty. The proposed SMO-UKF estimator accurately estimated aerodynamic torque and internal state by combining the robustness of SMO with the nonlinear estimation performance of UKF, while the fatigue-aware adaptive torque controller was designed to actively balance MPPT tracking performance and fatigue load reduction performance according to real-time operating conditions. Furthermore, the stability of the proposed estimator and controller was verified through Lyapunov-based analysis. Simulation results showed that the proposed SMO-UKF estimator exhibited superior estimation accuracy and response characteristics compared to existing techniques, and the proposed torque controller reduced DEL by up to 15.39% and torque standard deviation by up to 13.35% compared to existing OTC, while maintaining output power loss at less than 1%. Through this, it was confirmed that the proposed method can achieve an effective balance between the conflicting control objectives of maintaining power generation performance and reducing fatigue load. Furthermore, by maintaining stable performance even in high-volume environments, it is expected to contribute to reducing fatigue damage and maintenance costs in actual large-scale wind power systems. For actual application in wind turbines, further verification is required considering realistic constraints such as sensor resolution, actuator saturation, communication latency, and embedded controller performance. Additionally, verification through Hardware in the Loop (HIL) testing and actual wind turbine demonstration remains a task for future research.

Author contributions

Jun-Hee Lee: Conceptualization, methodology, formal analysis, visualization, writing – original draft; Ganesh Mayilsamy: Software, methodology, investigation; Baek-Soon Kwon: Investigation, methodology; Jae Hoon Jeong: Project administration, supervision, writing – review & editing. All authors have read and approved the final version of the manuscript for publication.

Use of Generative-AI tools declaration

The authors declare they have not used Artificial Intelligence (AI) tools in the creation of this article.

Acknowledgments

This research was supported by Korea Basic Science Institute (National research Facilities and Equipment Center) grant funded by the Ministry of Education (2023R1A6C101B042).

Conflict of interest

The authors declare that they have no conflict of interest.

References

1. J. G. Njiri, N. Beganovic, M. H. Do, D. Söffker, Consideration of lifetime and fatigue load in wind turbine control, *Renew. Energy.*, **131** (2019), 818–828. https://doi.org/10.1016/j.renene.2018.07.109
2. M. Ucar, M. Hmedi, E. Uzunoglu, E. Oguz, Fatigue load evaluation of multiple floating wind turbine systems, *Ocean Eng.*, **330** (2025), 121101. https://doi.org/10.1016/j.oceaneng.2025.121101
3. L. Fu, J. Liu, Y. Gao, Y. Zhou, F. Xu, X. Deng, Coordinative optimization for wind farms considering improved fatigue load index, *Int. J. Elec. Power*, **162** (2024), 110282. https://doi.org/10.1016/j.ijepes.2024.110282
4. L. Qi, M. Zhao, S. Wu, X. Zhang, P. Meng, Y. Zhao, et al., Adaptive torque feed-forward control for wind turbine MPPT considering predicted wind speed characteristics, *Int. J. Elec. Power*, **167** (2025), 110598. https://doi.org/10.1016/j.ijepes.2025.110598
5. Y. Wang, Y. Guo, D. Zhang, H. Liu, R. Song, Analysis and mitigation of the drive train fatigue load for wind turbine with inertial control, *Int. J. Elec. Power*, **136** (2022), 107698. https://doi.org/10.1016/j.ijepes.2021.107698
6. A. Safaeinejad, M. Rahimi, D. Zhou, F. Blaabjerg, A. sensorless active control approach to mitigate fatigue loads arising from the torsional and blade edgewise vibrations in PMSG-based wind turbine system, *Int. J. Elec. Power*, **155** (2024), 109525. https://doi.org/10.1016/j.ijepes.2023.109525

7. Z. Li, S. Tian, Y. Zhang, H. Li, M. Lu, Active control of drive chain torsional vibration for DFIG-based wind turbine, *Energies*, **12** (2019), 1744. https://doi.org/10.3390/en12091744
8. M. Rahimi, A. Beiki, Efficient modification of the control system in PMSG-based wind turbine for improvement of the wind turbine dynamic response and suppression of torsional oscillations, *Int. T. Electr. Energy*, **28** (2018), e2578. https://doi.org/10.1002/etep.2578
9. A. Beiki, M. Rahimi, An efficient sensorless approach for energy conversion enhancement and damping response improvement in permanent magnet synchronous generator (PMSG) based wind turbines, *Int. T. Electr. Energy*, **29** (2019), e2684. https://doi.org/10.1002/etep.2684
10. R. Rocha, A sensorless control for a variable speed wind turbine operating at partial load, *Renew. Energy*, **36** (2011), 132–141. https://doi.org/10.1016/j.renene.2010.06.008
11. Y. Wang, Y. Guo, W. Xu, Impact mechanism of frequency response on wind turbine fatigue load, *J. Renew. Sustain. Ener.*, **15** (2023). https://doi.org/10.1063/5.0132363
12. A. Cetrini, F. Cianetti, M. L. Corradini, G. Ippoliti, G. Orlando, On-line fatigue alleviation for wind turbines by a robust control approach, *Int. J. Elec. Power*, **109** (2019), 384–394. https://doi.org/10.1016/j.ijepes.2019.02.011
13. J. A. Collins, *Failure of materials in mechanical design: Analysis, prediction, prevention*, John Wiley & Sons, 1993.
14. X. Jin, W. Tan, Y. Zou, Z. Wang, Active disturbance rejection control for wind turbine fatigue load, *Energies*, **15** (2022), 6178. https://doi.org/10.3390/en15176178
15. A. Safaeinejad, M. Rahimi, D. Zhou, F. Blaabjerg, An efficient power control strategy for active mitigation of blade in-plane fatigue loading in PMSG-based wind turbines, *IET Renew. Power Gen.*, **18** (2024), 261–282. https://doi.org/10.1049/rpg2.12923
16. Q. Yao, Y. Hu, T. Zhao, Y. Guan, Z. Luo, J. Liu, Fatigue load suppression during active power control process in wind farm using dynamic-local-reference DMPC, *Renew. Energy*, **183** (2022), 423–434. https://doi.org/10.1016/j.renene.2021.10.069
17. L. Ren, C. Mao, Z. Song, F. Liu, Study on active disturbance rejection control with actuator saturation to reduce the load of a driving chain in wind turbines, *Renew. Energy*, **133** (2019), 268–274. https://doi.org/10.1016/j.renene.2018.10.041
18. H. Wang, Y. Liu, X. Wang, G. Guo, L. Wang, Dynamic synthetic inertial control method of wind turbines considering fatigue load, *Front. Energ. Res.*, **10** (2023), 1067896. https://doi.org/10.3389/fenrg.2022.1067896
19. J. Gallego-Calderon, A. Natarajan, Assessment of wind turbine drive-train fatigue loads under torsional excitation, *Eng. Struct.*, **103** (2015), 189–202. https://doi.org/10.1016/j.engstruct.2015.09.008
20. M. Ganesh, J. H. Jeong, A lightweight adaptive torque control of PMSG-based offshore wind turbines using a finite-step incremental search strategy for region-III operation under variable air density conditions, *Ocean Eng.*, **352** (2026), 124377. https://doi.org/10.1016/j.oceaneng.2026.124377
21. A. Sambas, A. Mohammadzadeh, S. Vaidyanathan, A. F. M. Ayob, A. Aziz, M. A. Mohamed, et al., Investigation of chaotic behavior and adaptive type-2 fuzzy controller approach for Permanent Magnet Synchronous Generator (PMSG) wind turbine system, *AIMS Math.*, **8** (2023), 5670–5686. https://doi.org/10.3934/math.2023285
22. A. K. Alsharidi, S. Rashid, S. K. Elagan, Short-memory discrete fractional difference equation wind turbine model and its inferential control of a chaotic permanent magnet synchronous transformer in time-scale analysis, *AIMS Math.*, **8** (2023), 19097–19120. https://doi.org/10.3934/math.2023975

23. H. Polinder, F. F. A. Van der Pijl, G. J. De Vilder, P. J. Tavner, Comparison of direct-drive and geared generator concepts for wind turbines, *IEEE T. Energy Conver.*, **21** (2006), 725–733. https://doi.org/10.1109/TEC.2006.875476
24. E. Gauterin, P. Kammerer, M. Kühn, H. Schulte, Effective wind speed estimation: Comparison between Kalman filter and Takagi–Sugeno observer techniques, *ISA T.*, **62** (2016), 60–72. https://doi.org/10.1016/j.isatra.2015.11.016
25. R. Rocha, A sensorless control for a variable speed wind turbine operating at partial load, *Renew. Energy*, **36** (2011), 132–141. https://doi.org/10.1016/j.renene.2010.06.008
26. O. Barambones, Robust wind speed estimation and control of variable speed wind turbines, *Asian J. Control*, **21** (2019), 856–867. https://doi.org/10.1002/asjc.1779
27. F. Golnary, K. T. Tse, Novel sensorless fault-tolerant pitch control of a horizontal axis wind turbine with a new hybrid approach for effective wind velocity estimation, *Renew. Energy*, **179** (2021), 1291–1315. https://doi.org/10.1016/j.renene.2021.07.112
28. J. Zhao, L. Mili, A theoretical framework of robust H-infinity unscented Kalman filter and its application to power system dynamic state estimation, *IEEE T. Signal Proces.*, **67** (2019), 2734–2746. https://doi.org/10.1109/TSP.2019.2908910
29. W. Xu, G. Zong, B. Niu, H. Wang, X. Zhao, Event-based fuzzy adaptive boundary Taylor decoupling control for parabolic PDE cascade systems: a novel nonlinear filters approach, *Fuzzy Set. Syst.*, **542** (2026), 109945. https://doi.org/10.1016/j.fss.2026.109945
30. W. Zhang, X. Zhao, B. Niu, G. Zong, Integral barrier Lyapunov functions-based adaptive fuzzy event-triggered fault tolerant control for PDE-ODE cascade systems with state constraints: W. Zhang et al., *Nonlinear Dynam.*, **114** (2026), 229. https://doi.org/10.1007/s11071-025-12081-4
31. M. Lara, F. Vázquez, I. Sandua-Fernandez, J. Garrido, Adaptive active generator torque controller design using multi-objective optimization for tower lateral load reduction in monopile offshore wind turbines, *IEEE Access*, **11** (2023), 115894–115910. https://doi.org/10.1109/ACCESS.2023.3325840
32. B. Liu, Q. Huang, L. Xu, W. Hu, A nonlinear drivetrain torsional oscillation damper for WTGs: Robust rejection of large disturbances with balanced noise immunity, *IEEE T. Sustain. Energ.*, **17** (2025), 1348–1363. https://doi.org/10.1109/TSTE.2025.3614712
33. X. Li, W. Wang, F. Fang, J. Liu, Z. Chen, Improving active power regulation for wind turbine by phase leading cascaded error-based active disturbance rejection control and multi-objective optimization, *Renew. Energy*, **243** (2025), 122629. https://doi.org/10.1016/j.renene.2025.122629
34. S. Cheng, Y. Gao, J. Liu, C. Guo, F. Xu, L. Fu, An optimal control strategy considering fatigue load suppression for wind turbines with soft switch multiple model predictive control based on membership functions, *Energies*, **18** (2025), 4695. https://doi.org/10.3390/en18174695
35. Y. Wang, S. Zhu, R. Deng, B. Yang, P. Wang, S. Gu, Model predictive control of wind turbine based on deep-dive holistic observer of tower top IMU, *Appl. Energ.*, **392** (2025), 125996. https://doi.org/10.1016/j.apenergy.2025.125996
36. Z. Lin, Z. Chen, J. Liu, Q. Wu, Coordinated mechanical loads and power optimization of wind energy conversion systems with variable-weight model predictive control strategy, *Appl. Energ.*, **236** (2019), 307–317. https://doi.org/10.1016/j.apenergy.2018.11.089
37. Q. Yao, Y. Hu, H. Deng, Z. Luo, J. Liu, Two-degree-of-freedom active power control of megawatt wind turbine considering fatigue load optimization, *Renew. Energy*, **162** (2020), 2096–2112. https://doi.org/10.1016/j.renene.2020.09.137

38. A. Safaeinejad, M. Rahimi, D. Zhou, F. Blaabjerg, A sensorless active control approach to mitigate fatigue loads arising from the torsional and blade edgewise vibrations in PMSG-based wind turbine system, *Int. J. Elec. Power*, **155** (2024), 109525. https://doi.org/10.1016/j.ijepes.2023.109525
39. M. Ganesh, S. R. Lee, J. H. Jeong, Y. H. Joo, An improved direct predictive speed control for three-level NPC converter fed PMSG-based offshore wind turbine system with minimum computation, *Ocean Eng.*, **314** (2024), 119705. https://doi.org/10.1016/j.oceaneng.2024.119705
40. M. Nasiri, J. Milimonfared, S. H. Fathi, A review of low-voltage ride-through enhancement methods for permanent magnet synchronous generator based wind turbines, *Renew. Sust. Energ. Rev.*, **47** (2015), 399–415. https://doi.org/10.1016/j.rser.2015.03.079
41. A. A. Basheer, J. W. Park, J. H. Jeong, Robust power extraction in offshore permanent magnet vernier generator wind turbines using noise-resilient wind forecasting and anti-chattering control, *Control Eng. Pract.*, **168** (2026), 106695. https://doi.org/10.1016/j.conengprac.2025.106695
42. S. J. Julier, J. K. Uhlmann, *New extension of the Kalman filter to nonlinear systems*, Proc. SPIE 3068, Signal processing, sensor fusion, and target recognition VI, 1997. https://doi.org/10.1117/12.280797
43. H. K. Khalil, J. W. Grizzle, *Nonlinear systems*, Vol. 3. Upper Saddle River, NJ: Prentice Hall, 2002.
44. J. A. Moreno, M. Osorio, Strict Lyapunov functions for the super-twisting algorithm, *IEEE T. Automat. Contr.*, **57** (2012), 1035–1040. https://doi.org/10.1109/TAC.2012.2186179
45. H. J. Sutherland, *On the fatigue analysis of wind turbines*, Technical Report, Sandia National Labs., US, 1999. Available from: http://www.sars-expertcom.gov.hk/english/reports/reports.html.